8-2017

Dewetting Properties of Ag-Ni Alloy Thin Films

Benjamin Scott Wolf
University of Tennessee, Knoxville, bwolf2@vols.utk.edu

To the Graduate Council:

I am submitting herewith a thesis written by Benjamin Scott Wolf entitled "Dewetting Properties of Ag-Ni Alloy Thin Films." I have examined the final electronic copy of this thesis for form and content and recommend that it be accepted in partial fulfillment of the requirements for the degree of Master of Science, with a major in Materials Science and Engineering.

Philip D. Rack, Major Professor

We have read this thesis and recommend its acceptance:

Jason D. Fowlkes, Claudia J. Rawn

Accepted for the Council:
Dixie L. Thompson

Vice Provost and Dean of the Graduate School

(Original signatures are on file with official student records.)

Dewetting Properties of Ag-Ni Alloy Thin Films

A Thesis Presented for the

Master of Science

Degree

The University of Tennessee, Knoxville

Benjamin Scott Wolf

August 2017

Acknowledgements

First, I would like to thank Dr. Philip Rack for his guidance, input, and funding during the entirety of this project. He has been an invaluable asset during the last two years and I cannot thank him enough. Secondly, I would like to thank Dr. Joo Hyon Noh and Dr. Yueying Wu for their willingness to work with me and for teaching me how to properly conduct research. The time I spent with Dr. Wu over the last year is a memory I will always cherish and her teachings will undoubtedly help me throughout my career. The staff members at the Center for Nanophase Materials Science at Oak Ridge National Laboratory deserve a huge thanks for providing unparalleled assistance and patience as I attempted to break every tool in their clean room. Thank you to Dr. Chris Hartnett for always being open to dewetting discussions and for not beating me too badly on the golf course. To Dr. Tom Moore, thank you for introducing me to science, awakening my love for entrepreneurship, and always being open to throwing around new ideas no matter what time of night. Thank you to my mother, Mrs. Darlene Wolf-Moore. Without your fervent love and support I would not be where I am today. Your passion for knowledge and love for others is infectious and I thank you for instilling these things in me at a young age. To my girlfriend Katie, thank you for successfully navigating our long-distance relationship over the past 2 years, putting up with my random science ramblings over FaceTime, and picking me up when I am down. You are a real-life example that kindness, intelligence, and hard-work can take you far in this world. Finally, thanks to Dr. Jason Fowlkes and Dr. Claudia Rawn for their valuable insight and for agreeing to be on my thesis committee.

Abstract

In this study, pulsed laser induced dewetting of both patterned and continuous Nickel (Ni)-Silver(Ag) thin films was investigated extensively as a novel way to perform directed assembly of nano-particles. First, continuous Ni-Ag thin film dewetting was studied on both bulk and TEM (Transmission electron microscope) membrane substrates at a variety of compositions to better understand the dewetting dynamics of the Ni-Ag system. Then, patterned Ni-Ag thin film dewetting was studied on both bulk and TEM membrane substrates to understand how different patterns and thin film configurations effect nano-particle distribution and formation. All of this work was done in anticipation of the reception of a laser TEM attachment which will allow for in-situ pulsed laser induced dewetting experiments. Our results show that directed assembly of nano-particles is possible by using pulsed laser induced dewetting and that a variety of nano-particle formations and structures can be achieved through this method.

Table of Contents

List of Tables

List of Figures

Chapter 1 Introduction

1.1 Pulsed Laser Induced Dewetting

The idea of self-assembled structures and systems to combat the scaling challenges faced in the fields of microelectronics and materials science was inspired by many systems found in nature including the assembly of schools of fish in the ocean, flocks of birds in the sky, herds of wild animals, and oil droplets in water [1, 40]. Self-assembled nanoparticles can be used as the building blocks for applications such as tunable optics, nano-plasmonics, fuel-cells, magnetics, catalysis, nano-photonics, transparent conductors, chemical and biological sensors, surface enhanced Raman spectroscopy, and quantum dots [2, 3, 6-9]. These self-assembled nanoparticle structures are of great interest to the scientific community due to their unique properties, quantum behavior, and the ultimate goal of being able to manufacture products using a bottom-up approach [4]. The topic of interest for this paper is thin film dewetting on a solid substrate and this type of dewetting is accomplished through two different mechanisms: nucleation and growth of holes and spinodal dewetting [5]. Dewetting of continuous metal films undergoes three successive stages: nano-hole formation due to rupture of the film, then transport/growth of the hole rims due to mass and energy transfer, and lastly the decay of the coalesced rims into nanoparticles via a Rayleigh-Plateau mechanism [6]. These stages are featured in figure 1.1.

1.1.1 Nucleation Theory

The process of nucleation describes a purely thermodynamic model which can be thought of as the first step in phase transition. Nucleation can be broken into two categories: homogeneous nucleation which describes a spontaneous and random process that requires a supercritical state and heterogeneous nucleation which occurs at a nucleation site, similar to seeded-crystal growth. Assuming spherical symmetry, the Gibbs free energy of a cluster can be defined as:

$$\Delta G = -\frac{4}{3}\pi r^3|\Delta G_v| + 4\pi^2\gamma. \quad (1.1)$$

Here, r is the radius, $|\Delta G_v|$ is the difference in Gibbs bulk free energy per unit volume, and γ is the surface energy per unit area. The positive and negative terms in the equation lead to a maximum in the Gibbs free energy curve known as the critical radius. The value of the critical radius can be deciphered by solving equation 1.1 for $\frac{d\Delta G}{dr} = 0$, which gives:

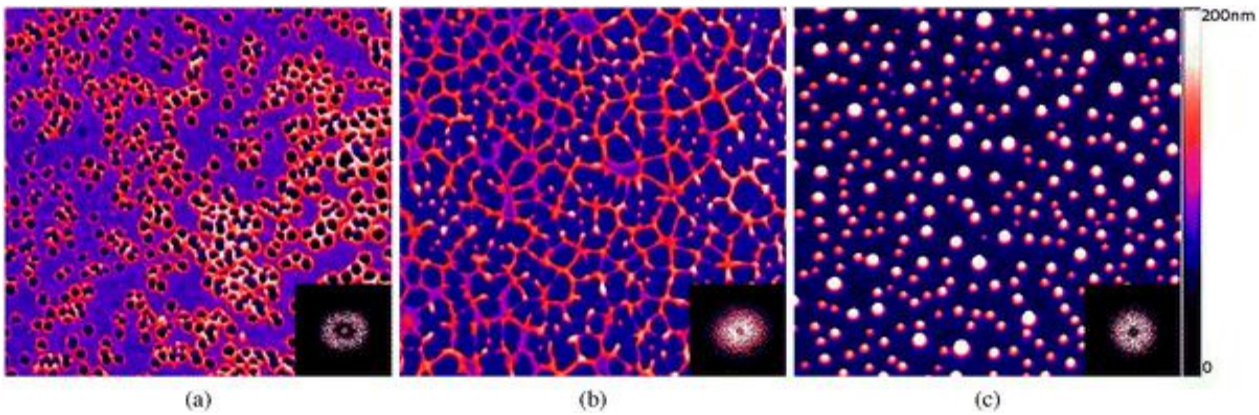

Figure 1. 1- Dewetting evolution of an ultrathin Ag metal film on SiO2 substrates. (a) Nano-hole formation due to initial rupture of the film. (b) Film growth/ rivulet formation due to mass and energy transmissions. (c) Decay of holes into nanoparticles.

"H. Krishna, N. Shirato, C. Favazza, and R. Kalyanaraman, "Energy driven self-organization in nanoscale metallic liquid films," *Phys. Chem. Chem. Phys.*, vol. 11, no. 37, pp. 8136–8143, Sep. 2009."

$$r_c = \frac{2\gamma}{|\Delta G_v|}. \quad (1.2)$$

Then, the expression for critical free energy, ΔG_c can be derived by replacing r from equation 1.1 with r_c:

$$\Delta G_c = \frac{16\pi\gamma^3}{|\Delta G_v|^2}. \quad (1.3)$$

The value of the volume free energy can be solved for using:

$$\Delta G_v = -\frac{K_B T ln(S)}{V_m}, \quad (1.4)$$

where T is temperature, K_B is Boltzman's constant, V_m is molar volume, and S is the supersaturation of solution [7]. Since nucleation relies on the formation of a critical nucleus, the timescale for nucleation is typically much larger than that of the microscopic dynamics of the system and can be described by:

$$rate = \rho Z j exp\left(-\frac{\Delta G_c}{K_B T}\right), \quad (1.5)$$

Where ρ is the number density of molecules, j is the rate at which molecules attach to the nucleus causing it to grow, and Z is the Zeldovich factor [8]. Heterogeneous nucleation typically occurs more often than homogeneous nucleation because it requires a lower activation energy. Although it is assumed that both kinds of nucleation occur simultaneously and parallel during nanoparticle synthesis [7].

In thin films specifically, material accumulates at the perimeter of nucleated holes by growing an elevated rim around them [9]. This rim grows in diameter with time and will eventually break into droplets with sizes and distribution of the droplets based on the initial film thickness, liquid viscosity, surface tension of the film, and cleanliness of the substrate. As the initial droplets are formed, they drain the liquid from the nucleation rim and grow [10]. The holes initiate at randomly distributed film defects due to heterogeneous nucleation [11].

1.1.2 Spinodal Theory

The second mechanism used to describe dewetting of thin films is Spinodal dewetting and is defined as "A clustering reaction in a homogeneous, supersaturated solution (solid or liquid) which is unstable against infinitesimal fluctuations in density of composition. The solution therefore separates spontaneously into two phases, starting with small fluctuations and proceeding with a decrease in the Gibbs energy without a nucleation barrier" [12]. An artifact of Spinodal dewetting is highly ordered spatial patterns of nanoparticles that can be controlled by understanding thermophysical material properties such as interfacial tension, contact angle with the substrate, fluid viscosity, and long range dispersion forces such as Van Der Waal's forces [13]. The process of spinodal dewetting begins when the amplitude of the surface fluctuations peaks or spikes exceed the dimension of the film causing the film to begin to dewet. Next, the film ruptures and forms randomly distributed holes where the distance between these holes is proportional to the square of the thickness of the film. These holes grow and form an interconnected mesh of rivulets which eventually are subject to Rayleigh-Plateau instabilities where the unstable perturbations eventually decay into nanoparticle droplets [14].

The first parameter to consider when trying to model spinodal dewetting is the wettability of a drop of film fluid in the presence of bounding fluids. This can be done using the Young-Dupre equation,

$$\gamma_{fb}\cos\theta + \gamma_{sf} = \gamma_{sb}, \qquad S = \gamma_{sb} - \gamma_{sf} - \gamma_{fb} = \gamma_{fb}\cos\theta - \gamma_{fb}, \tag{1.6}$$

where S is the total spreading coefficient, θ is the equilibrium contact angle of the drop, γ_{sb} is the total interfacial tension between the substrate and the bounding fluid, γ_{sf} is the interfacial tension between the substrate ad the film fluid, and γ_{fb} is the interfacial tension between the film fluid and the bounding fluid. Figure 1.2 shows the interfacial tensions mentioned above. A negative spreading coefficient, S, results in destabilization of the film and will cause dewetting [14].

The second set of important parameters when modeling spinodal theory are time and length scales of the observed dewetting pattern. These can be modeled using lubrication theory which "provides a relationship between the mass flux (which can be related to temporal variations in film height) and the effective pressure gradient, which for a thin film could result from perturbations that produce interface curvature, and disjoining pressure due to long-range intermolecular forces such as Van Der Waals interactions" [13]. Intermolecular forces are dominant in thin films. Two mechanisms compete during dewetting: Laplace pressure, which is a measure of the surface tension trying to keep the film flat, and the Van Der Waals disjoining pressure which describes the likelihood of a film to adjust its thickness in order to minimize free energy. Together, these two forces determine the shape of a film on a solid substrate. The Laplace pressure can be described by [14]:

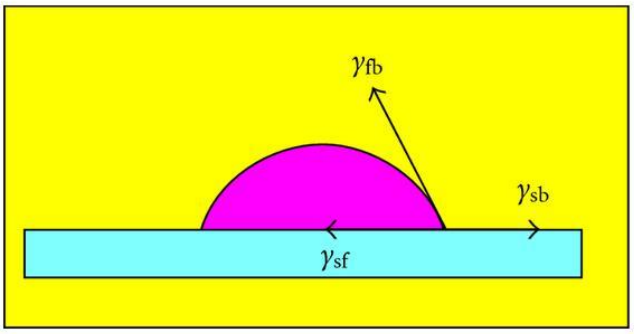

Figure 1. 2- Interfacial tensions on a drop of material on a substrate.

"S. P. Singh, "Spinodal Theory: A Common Rupturing Mechanism in Spinodal Dewetting and Surface Directed Phase Separation (Some Technological Aspects: Spatial Correlations and the Significance of Dipole-Quadrupole Interaction in Spinodal Dewetting)," *Adv. Condens. Matter Phys.*, vol. 2011, p. e526397, May 2011."

$$P_L = \gamma\left(\frac{d^2h(x,t)}{dx^2}\right), \quad (1.7)$$

where P_L is the Laplace pressure, γ is the interfacial tension of the film bounding interface, and h(x,t) is the variation in height of the film at different position x and time t which can be described by:

$$h(x,t) = h_0 + \exp(Iqx) * \exp(Rt), \quad (1.8)$$

where h_0 is the initial thickness, q is the wave vector along the x axis and R is the growth rate. The Van Der Waals disjoining pressure can be described by:

$$\Pi = \frac{A}{6\pi h^3}, \quad (1.9)$$

where A is the Hamaker constant and h is the instantaneous film thickness. If the Hamaker constant is negative, then the film will tend to get thinner. The Hamaker constant plays an important role as it determines which phase the liquid will take on the surface of your substrate and can be defined as:

$$A = \pi^2 C \rho_1 \rho_2 , \quad (1.10)$$

where C is the coefficient of particle-particle interaction, and ρ_1 and ρ_2 are the number densities of the two interacting particles. Equation 1.10 allows for the determination of the interaction parameter, C, by using the Van Der Waals pair potential equation:

$$\omega(r) = \frac{-C}{r^6} , \quad (1.11)$$

where r is the distance between the two particles. The above questions can be used to derive the characteristic wavelength, Λ, as a function of film thickness, h, which is given by:

$$\Lambda = \sqrt{\frac{16\pi^3\gamma}{A}}h^2 \,. \tag{1.12}$$

Finally, the time scale, τ_D, that is associated with growth perturbations of wavelength Λ can be defined as:

$$\tau_D = \frac{96\pi^3\gamma\eta h^5}{A^2}\,, \tag{1.13}$$

where η is the viscosity of the liquid.

The spinodal dewetting mechanism dominates dewetting in thin metal films ranging from 1 to tens of nanometers. In thin metal films, this mechanism can be described by breakup of the film through unstable thermal fluctuations followed by the eventual formation of nanodroplets that are spatially distributed. The spatial distribution of the particles is determined by the fastest growing surface perturbation wavelengths. The effective potential between the liquid film and substrate greatly influences the spinodal breakup of the film. The liquid-phase dewetting dynamics of thin metal films are difficult to observe in-situ because of nanoscale length and time scales due to low viscosity and high surface energy of the liquid film. McKeown et al. used pump-probe electron microscopy techniques to observe in situ the dewetting of thin nickel films irradiated with nano-second laser pulses. Through thickness-dependent and correlated time and length scale measurements, they were able to determine that spinodal instabilities do indeed drive the dewetting process in this metallic films [15].

1.1.3 Rayleigh Plateau Theory

Rayleigh-Plateau theory describes how a liquid filament of water collapses into droplets [16]. Capillary and interstitial forces govern the breakup of a fluid jet suspended in air, but in the case of liquid film dewetting, the substrate-stream interaction potential must be considered. The substrate-stream interaction controls the contact angle of the liquid metal stream during dewetting. A modified version of the Rayleigh-Plateau theory was derived to include the substrate-stream interaction potential and this can be used to estimate a dispersion curve for the nanodroplets on the substrate. Understanding and tuning the modified Rayleigh Plateau theory is crucial to controlling the self-assembly pathway during dewetting [17].

1.2 Pulsed Laser Induced Dewetting of Metal Films

Pulsed laser induced dewetting of metal films has been studied for a variety of different metals and metallic alloys in the past several years. McKeown et al. studied copper cobalt alloys because of the systems immiscibility and to understand the effects of combining a strong magnet (Co) with a strong conductor (Cu) in a single nanoparticle. They were able to show that pulsed laser induced dewetting of Co-Cu thin films is an effective method for producing Co-Cu core-shell nanoparticles with tunable sizes ranging from tens to several hundred nanometers. They were also able to show that pulsed laser induced dewetting is a plausible method for bottom-up self-assembly without the need for any lithographic processes [18].

Favazza et al. studied the pattern evolution of thin Co films ranging in thickness from 1 to 8nm through laser induced dewetting. They observed that upon initial breakup of the film there is formation of cellular patterns which evolve into polygons that then form nanoparticles with unimodal size distribution and short range order between nearest neighbor spacing. They attributed the special ordering of the nanoparticles to a hydrodynamic thin film instability and again showed pulsed laser induced dewetting as a possible method for bottom-up self-assembly [13].

Fowlkes et al. researched the effects of adding synthetic perturbations to thin nickel strips in order to observe self- versus directed- assembly of nanoparticles via pulsed laser induced dewetting. They found that by adding synthetic sinusoidal perturbations onto the lateral surfaces of the thin film strip they could control the nanoparticle diameter and pitch. The perturbations on the strip caused unstable varicose oscillation of the rivulet during retraction (the intermediate phase between strip and particle) which allowed the strip to overcome the modes predicted by Rayleigh-Plateau instability [19].

Krishana et al. used laser induced dewetting to understand the dewetting morphology of ultrathin silver films. They showed that films less than 9.5nm thick formed bi-continuous structures during the intermediate stages of dewetting and films greater than 11.5nm formed regularly sized holes during the intermediate stages of dewetting. Through this study they were able to determine the morphological transition thickness for silver which is useful when forming complex silver nanomorphology’s in a consistent manner [20].

Wu et al. studied the optical properties of Cu-Ni nanoparticles produced via pulsed laser induced dewetting of metal films. They used continuous Cu-Ni alloy thin films ranging from 2-8nm to compare the optical properties before and after laser induced dewetting and found that the copper rich nanoparticles formed after the laser ablation revealed a signature absorption peak suggestive of a plasmon peak. The observed plasmon peak was shown to be tunable by a red-shift with increasing nanoparticle size and blue-shifts with increasing nickel concentration [21].

Wu et al. also studied the directed assembly of nanomaterials by pulsed laser induced dewetting in lithographically patterned copper thin films. They found that this combination of top-down lithography and bottom-up self-assembly can create nanoparticle arrays with controllable size, composition, and symmetry. They also proved that the particle size after laser exposure can be

smaller than the patterned lithographic geometry which could lead to the synthesis of advanced nanomaterials [22].

1.3 Ag-Ni System

Silver nanoparticles have been in use for decades with applications such as acting as an anti-bacterial agent in both the health and food storage industries as well as in different environmental applications. They are also of interest because of their ability to catalyze different chemical reactions, act as sensors for different molecules, and display unique optical properties such as surface plasmon resonance[23]. Nickel nanoparticles have also been of interest over the last few decades due to their unique properties and applications in optical, electronic, catalytic, and magnetic materials[24]. Bimetallic nanoparticles have shown increased functionality when compared to their monometallic components in properties such as magnetic, electronic, biological, and catalytic properties[25]. Silver-nickel particles have gathered interest for usage in catalysts, electronic contacts, switches, conductor material plating, electromagnetic wave absorbers, surface plasmon resonators, optical limiting, photonics and nickel based conductive pastes [25].

Silver nickel nanoparticles typically form in a core-shell structure, featured in figure 1.3, in which both the nickel cores and silver shells have a face centered cubic (fcc) structure [26]. Core shell nanoparticles offer tailorable properties due to their ability to have both their cores and shells tuned in distinct ways [27].

Nickel-silver nanoparticles can be synthesized in a variety of chemical processes including wet chemical reduction in $C_{14}H_{42}BrN$ matrix, reduction of silver nitrate and nickel nitrate with sodium borohydride in water-in-oil microemulsions of water/polyoxythylene, nonylphenol, and polyoxyethylene nonylphenol/n-heptane, successive hydrazine reduction of metal salts in ethylene glycol, coprecipitation of alloyed nanoparticles from the organic and aqueous phase [22]. In this thesis we will focus on a so called pulsed laser induced dewetting process [27] of Ni-Ag films.

1.3.1 Nickel Silver Phase Diagram

The silver-nickel phase diagram featured in figure 1.4 has a eutectic reaction at 960 ^{o}C and a monotectic reaction at 1435 ^{o}C. Although both nickel and silver have fcc crystal structures and a small difference in atomic radii, their solubilities are very limited. This leads to a miscibility gap in both the solid and liquid phase of the binary system which leads to phase separation of the alloy in both the liquid and solid phase[28].

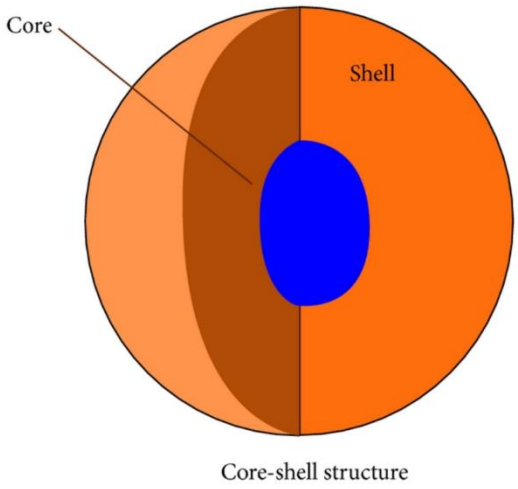

Figure 1. 3- Schematic of a core shell nanoparticle.

"K. S. Kumar, V. B. Kumar, and P. Paik, "Recent Advancement in Functional Core-Shell Nanoparticles of Polymers: Synthesis, Physical Properties, and Applications in Medical Biotechnology," *J. Nanoparticles*, vol. 2013, Jan. 2013."

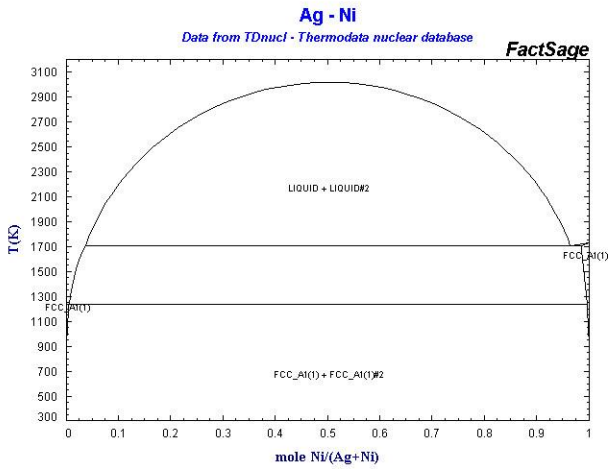

Figure 1. 4- Binary nickel silver phase diagram.

"SGTE - Scientific Group Thermodata Europe, "Ni-Ag Binary Phase Diagram." [Online]. Available: http://www.crct.polymtl.ca/sgte/index.php?what=1&databases=1&nobl=1. [Accessed: 01-Mar-2017]."

1.4 Electron Beam Lithography

Electron beam lithography (EBL) is used during nanofabrication to pattern structures down to sub 10 nanometer dimensions. At the most basic level, EBL describes the exposure of a highly-focused electron beam which modifies the solubility of a resist material that is later developed to form a pattern. The benefits of EBL include its extremely high resolution capabilities and its flexibility to work on a variety of materials and create almost any pattern. The main disadvantage of EBL is it's speed; EBL is orders of magnitude slower than optical lithography because it is a serial exposure process rather than a parallel or flood exposure of many patterns at one time [30, 31]. For this work, EBL was used to pattern different nanostructures that were subsequently processed via pulsed laser induced dewetting. The EBL tool allowed us to change the size, shape, and spacing of our nanostructures to better understand the effects these physical changes had during pulsed laser induced dewetting formation of ordered nanoparticle arrays. The main components of the EBL tool are featured in figure 1.5.

1.5 Laser Heating

The beam used in this study used krypton fluoride excimer as the lasing gas and the beam intensity has a Gaussian distribution in the vertical and horizontal directions. The heat flow experienced across the surface of a sample can be assessed using the conduction heat equation [30]:

$$\rho C_p \frac{\partial T}{\partial t} - \nabla(k\nabla T) = Gt\,, \tag{1.14}$$

where ρ is the material density, C_p is the specific heat capacity, ∇ is the gradient operator, T is the temperature, t is the time, k is the thermal conductivity, and Gt is the heat source distribution in the Z direction (depth). This interpretation of heat flow across the surface can be taken a step further by considering the enthalpy, H, relationship in the system which can be described using:

$$\Delta H = mC_p\Delta T\,, \tag{1.15}$$

where m is the mass of the material and Δ denotes a change in the parameter it proceeds. Equation 1.15 can be rearranged in terms of unit volume, where the mass is replaced by density and the enthalpy is now in terms of unit volume:

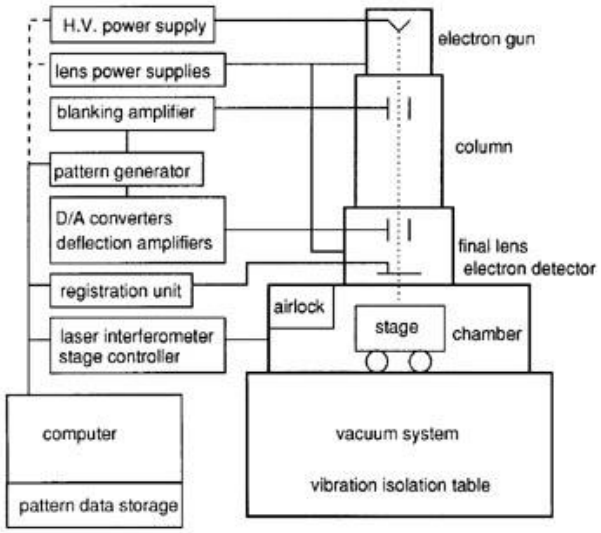

Figure 1. 5- Schematic showing the main components present in an EBL system.

"M. McCord and M. Rooks, "SPIE Handbook, Volume 1: Microlithography, Section 2.1." [Online]. Available: http://www.cnf.cornell.edu/cnf_spie1.html#2.1.1."

$$\Delta H_v = \rho C_p \Delta T\ , \tag{1.16}$$

The negative sign in equation 1.14 represents the idea that heat flows from hot to cold against the temperature gradient. Heat entering a small volume must either flow through to the other side or oppositely change the enthalpy of the system, which can be mathematically represented by the divergence operator, ∇,

$$\nabla \tilde{Q} = -\frac{dH_v}{dt}, \tag{1.17}$$

where $\tilde{Q} = {}^{dQ}/_{dt}$ or the rate of flow of heat. A positive divergence translates to a net loss of heat within the system (cooling) and a negative divergence translates to a net gain of heat within the system (heating). There is another source of energy in the form of absorbed optical radiation, S(z) in the z-direction which must contribute to the change in enthalpy:

$$\mathrm{S(z)} - \nabla \tilde{Q} = \frac{dH_v}{dt}. \tag{1.18}$$

The amount of energy absorbed from optical radiation, S(z), can be derived from the law of optics:

$$I_T = I_O(1 - R), \tag{1.19}$$

where I_O is the intensity of the laser beam, R is the reflectivity, and I_T is the intensity transmitted to the surface. There is an exponential decay of the optical density within the material which can be described by:

$$I(z) = I_T exp(-\alpha z), \tag{1.20}$$

where α is the optical absorption coefficient. These equations can be combined to define S(z) as:

$$S(z) = \alpha I(z) = \alpha I_O(1 - R)\exp(-\alpha z). \tag{1.21}$$

Thus, the equation:

$$\alpha I_O(1-R)\exp(-\alpha z) - \nabla\tilde{Q} = \frac{dH_v}{dt}, \tag{1.22}$$

is used when modeling laser heating.

1.6 Thin Film Deposition

Thin film deposition describes the technique of depositing a very thin film (from a few nanometers to 100 micrometers) onto a substrate or sample. Thin film deposition can be divided into two distinct categories: physical vapor deposition, which describes a group of technologies in which a material from a source is released then deposited using mechanical, electrochemical, or thermodynamic processes and chemical deposition, which describes a process in which a surface undergoes a chemical change due to a volatile fluid precursor, leaving a chemically deposited coating [31]. Both processes have advantages and disadvantages based on a variety of factors. Chemical vapor deposition requires a substrate to be at a much higher temperature than physical vapor deposition, but in turn this means that there is much less waste during chemical vapor deposition. Physical vapor deposition does not require a specialized precursor gas which allows for deposition of a much wider range of materials [32].

1.6.1 Radio Frequency Magnetron Sputtering

Sputtering describes a technique in which thin films are deposited onto a material (substrate) surface. During the sputtering process, a source material is eroded by accelerated ions created in a gaseous plasma. The ions eject neutral atoms, clusters, or molecules from the target material through a direct energy transfer. The neutral atoms will travel in a straight line until they come in contact with a substrate, thus creating a thin film. Powering this process with DC voltage results in the acceleration of free electrons away from the negatively charged electrode or cathode. These electrons collide with neutral gas atoms causing them to lose electrons and become positively charged ions. Next, the positively charged ions are attracted to the negatively charged cathode and thus bombard the surface of the target material (on top of the negatively charged cathode) causing ejection of the target materials atoms from the surface. During this process, free electrons can combine with the positively charged ions turning them back into neutral atoms. This can cause the electrons to return to ground state and thus release a photon which is the reason the plasma appears to glow. Figure 1.6 features the process described above.

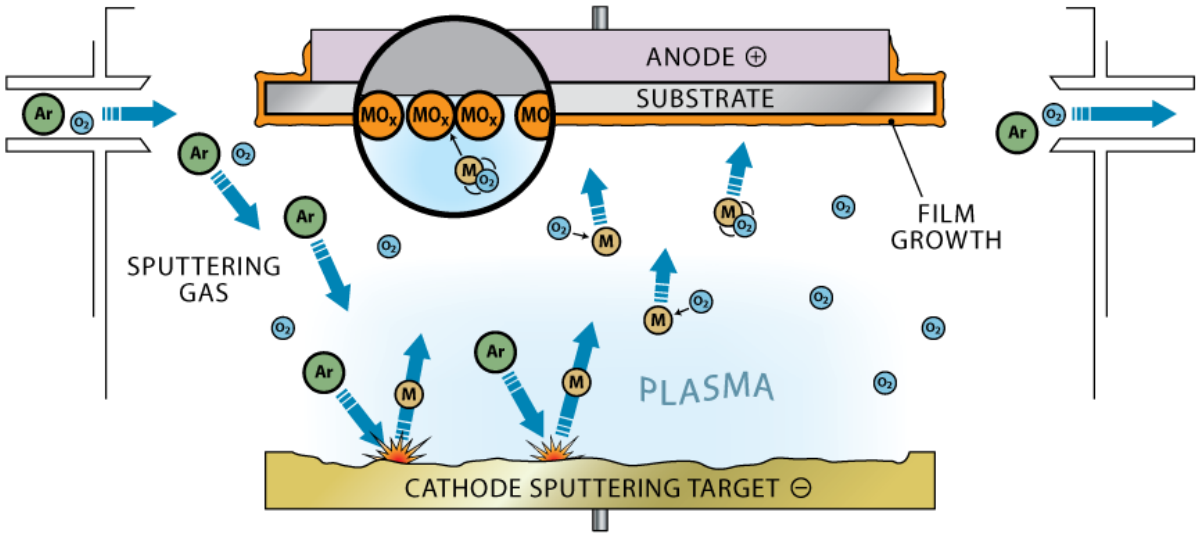

Figure 1. 6- Basic process of Sputter Deposition**.**

"Sputter deposition - LNF Wiki." [Online]. Available: http://lnf-wiki.eecs.umich.edu/wiki/Sputter_deposition."

A plasma, sometimes referred to as the fourth state of matter, describes a dynamic condition where neutral gas atoms, electrons, ions, and phonons exist simultaneously in balance. In order to maintain this dynamic state, an energy source is required (radio frequency in this thesis). This state can be created by introducing an electrode into a pre-pumped vacuum chamber then flowing a neutral gas into the chamber [33].

Radio frequency sputtering describes the process of alternating the electric potential of a current within a vacuum environment at radio frequencies. By alternating electric potentials, charge build-up is mitigated on the surface of the target material as electrons are attracted to the target during positive cycles (giving it a negative bias) and ion bombardment continues during the negative cycle. A radio frequency of 13. 56 MHz is used to accomplish this process in all RF power supply equipment.

RF sputtering offers several advantages over other sputtering methods depending on the application. RF sputtering can sustain a plasma at lower pressures which results in fewer ionized collisions and allows less disruptions during the coating process. Arcing is reduced during RF sputtering because the target material is cleaned during each current cycle. RF sputtering also reduces race track erosion on the target material which can lead to short-lived targets and cost users more money.

RF sputtering also has disadvantages that must be considered. Since RF sputtering uses radio waves instead of DC current, it requires much more voltage and has a slower deposition rate than other sputtering methods. This higher voltage can lead to overheating, the requirement for advanced circuitry, and more expensive power sources [34]. Figure 1.7 features a schematic of the RF magnetron sputtering tool.

Magnetron sputtering combats the problems of slow deposition rate and overheating by using magnets behind the cathode to create a magnetic field above the target material. This magnetic field is used to trap free electrons that are no longer free to strike the substrate material and have a higher probability of ionizing neutral gas molecules. This increases the number of ionized gas molecules to strike the target material and thus increases the number of atoms ejected from the target material. Figure 1.8 features the RF magnetron sputtering process described above.

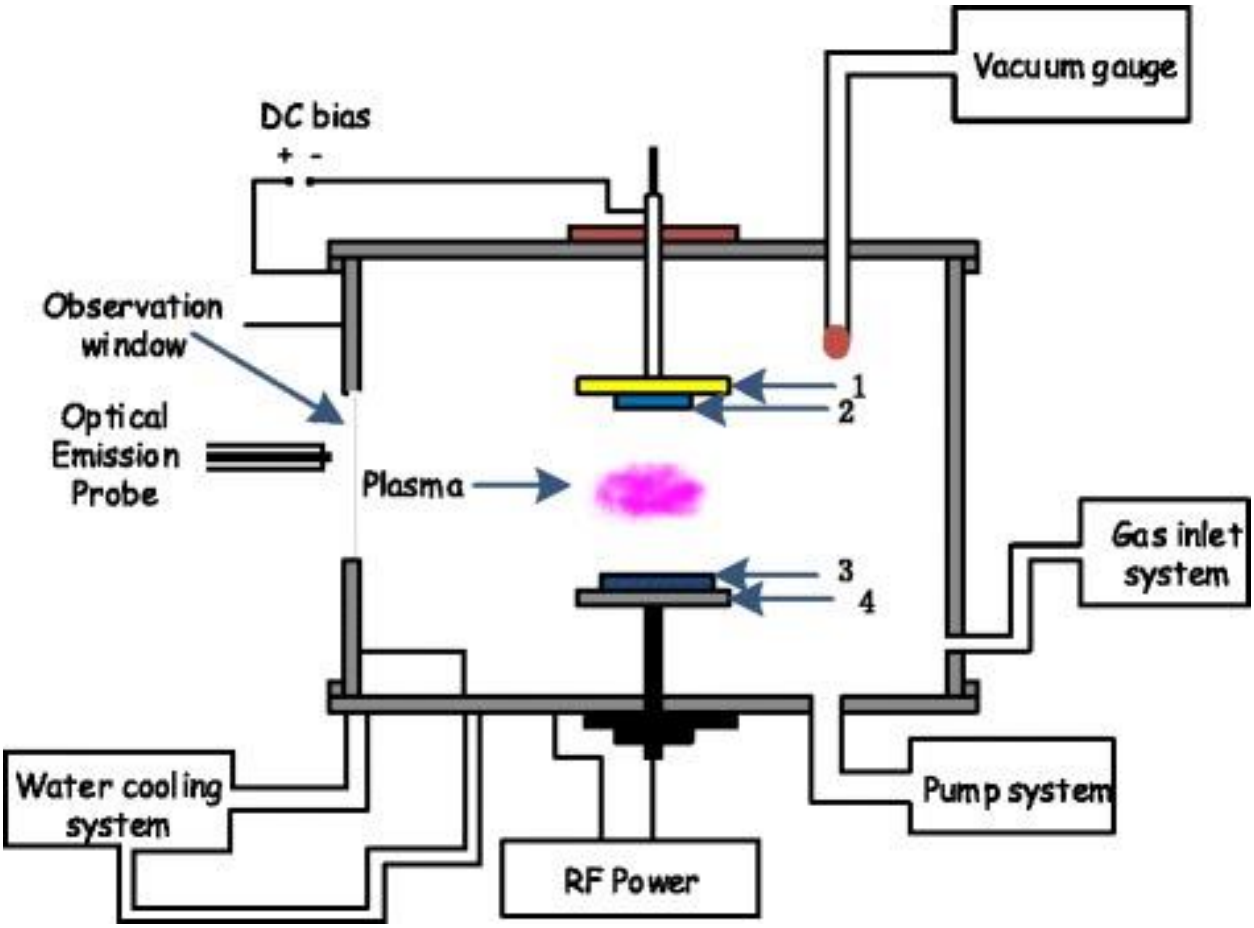

Figure 1. 7- Schematic drawing of a radio frequency magnetron sputtering tool.

"A. Majeed, J. He, L. Jiao, X. Zhong, and Z. Sheng, "Surface properties and biocompatibility of nanostructured TiO2 film deposited by RF magnetron sputtering," *Nanoscale Res. Lett.*, vol. 10, 2015."

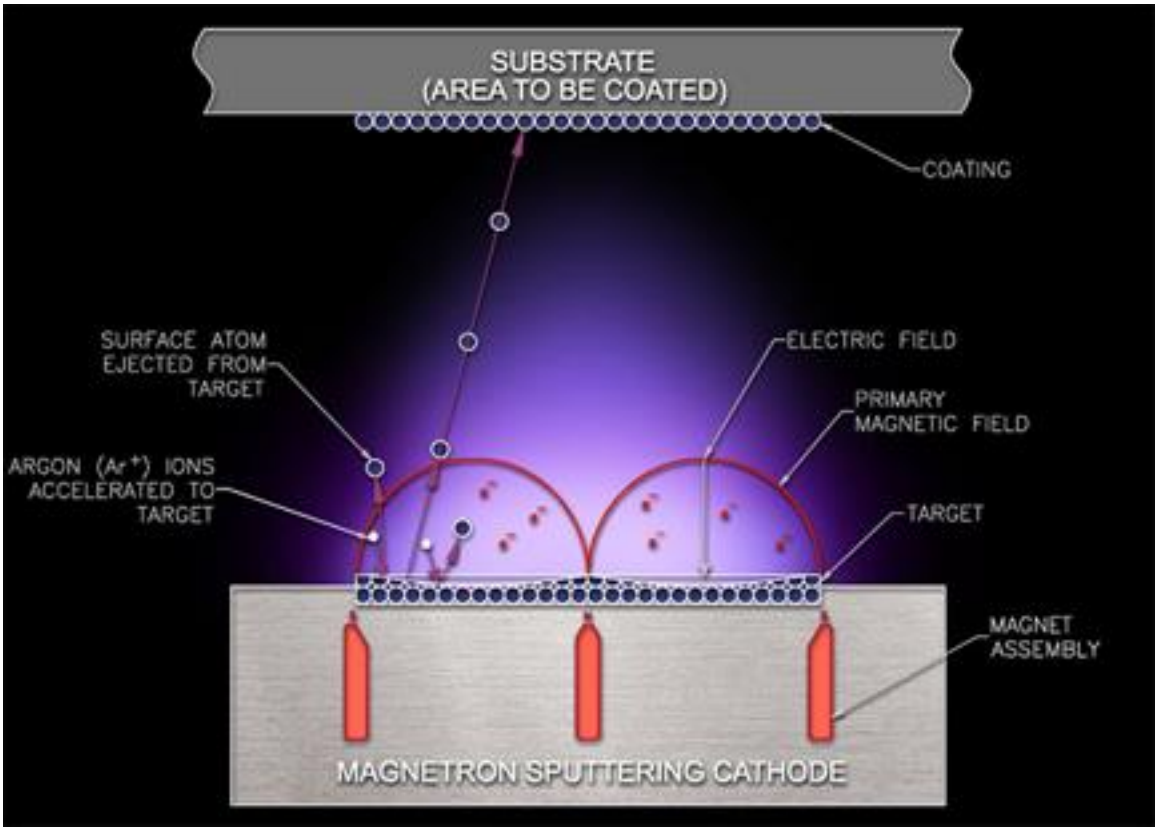

Figure 1. 8- Process caused by adding magnetrons to sputtering system.

NPTEL, "Advances in Spintronic Materials, Technology and Devices." [Online]. Available: http://nptel.ac.in/courses/115103039/module16/lec39/1.html.

Chapter 2 Experimental Protocol

2.1 Nickel Silver thin films deposition and Laser Irradiation

Nickel-silver layered and alloyed thin films were deposited using an RF magnetron sputtering system initially pumped to high vacuum (10^{-7} Torr). Nickel was deposited by using a 2-inch diameter nickel target (Kurt J. Lesker company) at an RF power of 30 watts and a 224 volt self-bias. Silver was deposited in a similar manner, but instead a 2-inch diameter silver foil target (Kurt J. Lesker company) was used at an RF power of 7 watts and a 120 volt self-bias. 25 sccm or Argon gas was flowed into the chamber at a 5 mTorr processing pressure. The sputtering rate for both metals was estimated at 1.5 nm/min **.** Figure 2.1 features a schematic detailing the sputtering target and substrate positions that will be referenced throughout this thesis.

All the thin films were irradiated in air by a KrF excimer laser with a 248 nm wavelength. The laser energy density ranged from 25 mJ/cm^2 to 500 mJ/cm^2 depending on the sample and the effects of varying laser energies on nano-particle formation properties was also studied. In the future, we hope to study in-situ dewetting of varying metallic thin films using a laser attachment on a transmission electron microscope.

2.2 Characterization

Many scanning electron microscopes (SEM) were used to capture the morphology during different stages of the dewetting process including a Zeiss Merlin SEM located at Oak Ridge National Lab, a Zeiss Auriga located at the Joint Institute for Advanced Materials (JIAM), and a Zeiss EVO MA 15 also located at JIAM.

Energy Dispersive Spectroscopy (EDS) analysis was obtained on the Zeiss Merlin SEM using a Bruker solid-state EDS detector to measure the relative compositions of particles and areas on the samples. All EDS measurements were operated at either 10 or 20kV accelerating voltage.

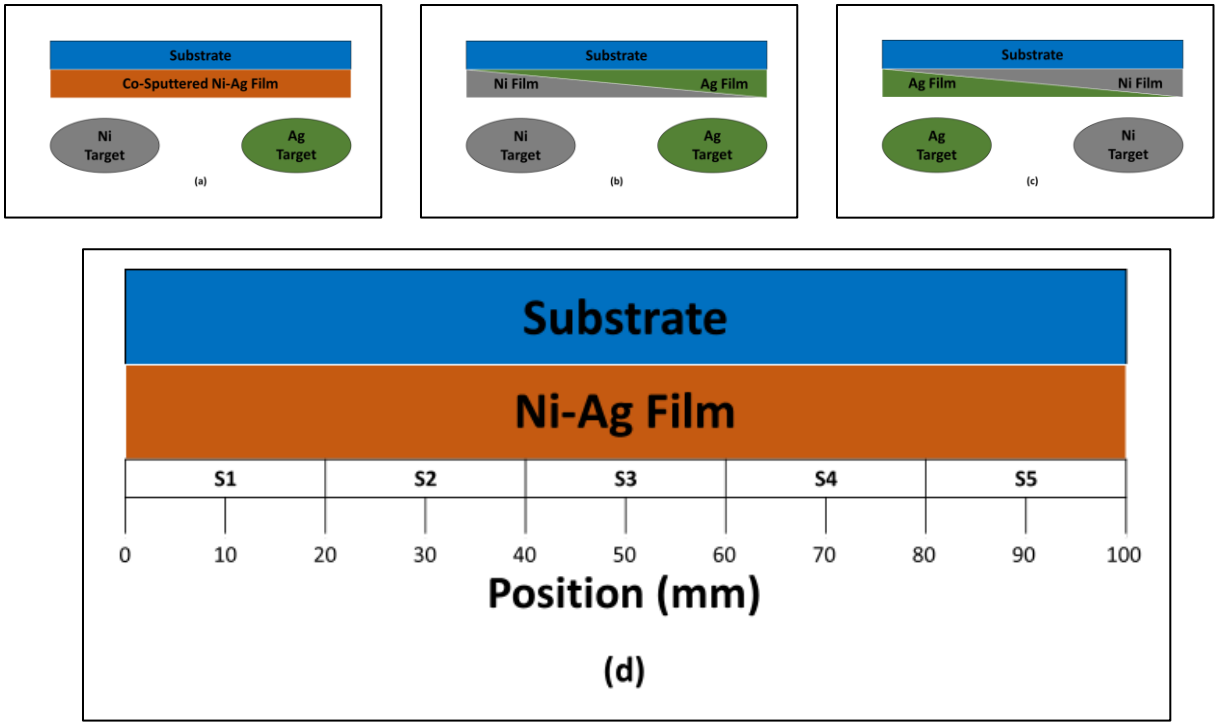

Figure 2. 1- (a-c) Schematics featuring three Ni-Ag thin film structures: (a) Co-sputtered, (b) Ni top Ag bottom, (c) Ag top Ni bottom. (d) Illustration featuring the Ni-Ag thin film surface with reference locations.

Chapter 3 Experimental Results

3.1 Continuous Film Dewetting on Bulk Substrates

To understand the initial dewetting mechanisms caused by the different interface forces, varying laser absorption and temperatures, and different liquid dynamics competing in the phase separation process of the nickel-silver system, many different experiments were conducted using continuous thin films deposited on bulk substrates. We began with pulsed laser induced dewetting on continuous thin films because our group has experience with these types of experiments. The details of these preliminary experiments are overviewed in the remainder of this section.

3.1.1 Substrate Effect Study

To understand the effects different substrates have on the dewetting process and the effects different laser energies have on the solid and liquid phase dynamics on varying substrates we fabricated three different samples: (1)12 nm co-sputtered continuous Ni-Ag film on 100 nm SiO_2 lasered at 150 mJ/cm^2 and 390 mJ/cm^2, (2)12nm co-sputtered continuous Ni-Ag film on 50nm Al_2O_3 lasered at 390 mJ/cm^2 and 500 mJ/cm^2, (3)12nm co-sputtered continuous Ni-Ag film on 30nm TiO_2 lasered at 390 mJ/cm^2 and 500 mJ/cm^2. We believed that the different surface tensions of the three oxide materials would cause a difference in the evolution of the dewetting process. Figure 3.1 features a summary of the results from our study.

These images show that the dewetting evolution was very similar on all thee substrates. Although there were some differences such as particle and hole density, we decided that they were not large enough to justify doing every future experiment on three different substrates. Thus, this lead to our decision to continue exploring various dewetting variables on SiO_2 and Si substrates.

3.1.2 Co-Sputtered Versus Bi-Layer Film Study

Next, we explored the effects of co-sputtered versus bi-layered film deposition on nano-particle formation during dewetting to better understand the interaction forces, laser absorption differences, and liquid dynamic competing phase separation processes that occur due to the different sputtering parameters. Three different Ni-Ag thin film configurations were deposited on 100 nm SiO_2 coated silicon substrates: (a, Ag on Ni) 10 nm (at center) Ni thin film covered by 10 nm (at center) Ag thin film, (b, co-sputtered) 20nm co sputtered Ni-Ag alloy thin film, and (c, Ni

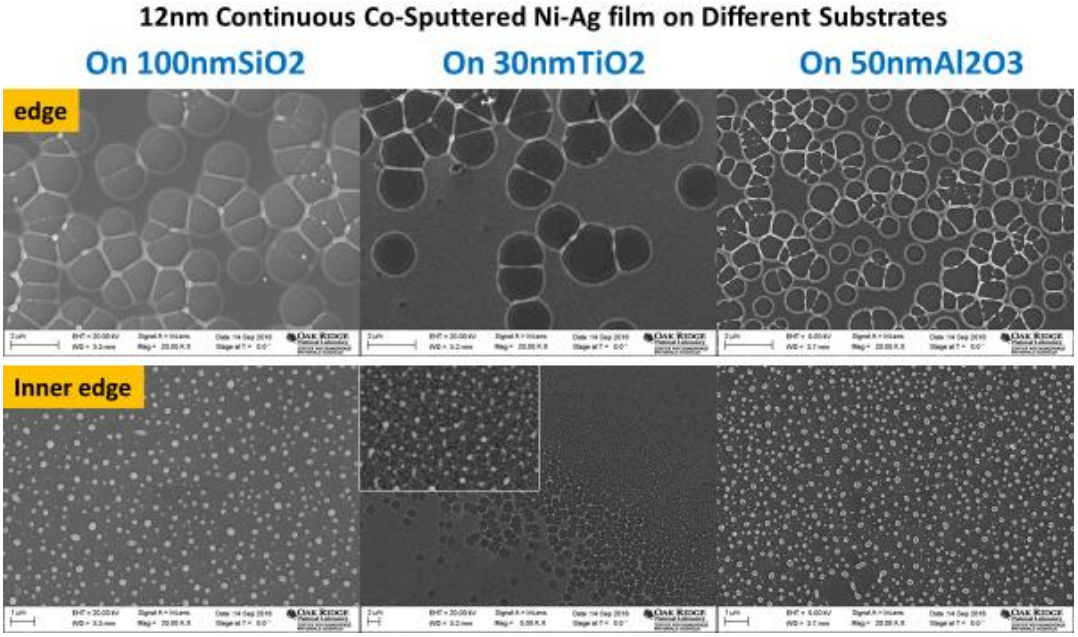

Figure 3. 1- SEM micrographs depicting the dewetting evolution of a 12nm continuous Co-Sputtered Ni-Ag film on SiO2, TiO2, and Al2O3.

on Ag) 10 nm (at center) Ag thin film covered by a 10nm (at center) Ni thin film. Figure 2.1 features a schematic detailing the sputtering target and substrate positions. For this study, we focused on position S3 (roughly 50/50 Ag-Ni) for consistency in our results. A summary of our results is featured in figure 3.2.

The SEM micrographs show that all three thin film deposition techniques formed similar sized particles with similar spatial density and the EDX line scans gave quantitative proof of core shell particle formation. The EDX line scans also show that regardless of the order that the thin films are deposited, the core-shell particles contain silver as the shell and nickel as the core. These results led us to our next study in which we researched what ratio of silver to nickel would lead to the formation of core-shell particles.

3.1.3 Ni-Ag Co-Sputtered Compositional Progression Study

In this study, we explored the effects on particle formation by varying the ratios of silver and nickel on each sample. To do this, we simultaneously sputtered 10 nm of nickel and 10 nm of silver on 100 nm SiO_2 coated silicon substrate. The sputtering guns were parallel to each end of the sample and thus formed a gradient (See figure 3.3 for clarification). Our substrate was roughly 10cm in length and after the thin film deposition was broken into five 2 cm pieces that we refer to as: S1 (roughly 90% Ag and 10% Ni), S2 (roughly 70% Ag and 30% Ni), S3 (roughly 50% Ag and 50% Ni), S4 (roughly 30% Ag and 70% Ni), and S5 (roughly 10% Ag and 90% Ni) (refer to Figure 2.1-(d) for clarification). A summary of our results is featured in Figure 3.4.

The SEM micrographs show the formation of particles with very similar sizes and spatial densities regardless of the thin film composition. The EDX line scans gave very interesting results, showing a very low Ni composition in the particles on S1, a slightly higher composition of Ni on S2, core shell particle formation and almost equal counts of Ag and Ni on S3, a very low composition of Ag on S4, and almost no Ag on S5. These results paired with prior results show that the best Ni-Ag core-shell particles are formed at a 50%-50% composition, regardless of the thin film deposition order.

3.2. Pattern Library

Based on previous experience, we used a large library of patterns to explore the physical interactions caused by dewetting of unique shapes and arrays. Layout Editor software was used to create our patterns. Below are images and details on the different patterns used in this study.

Our unit pattern features multiple arrays of circles with varying diameters (100nm, 200nm, 300nm, 400nm, and 500nm) and varying spaces between each circle (100nm, 200nm, and 300nm). An example of this pattern is featured in figure 3.5.

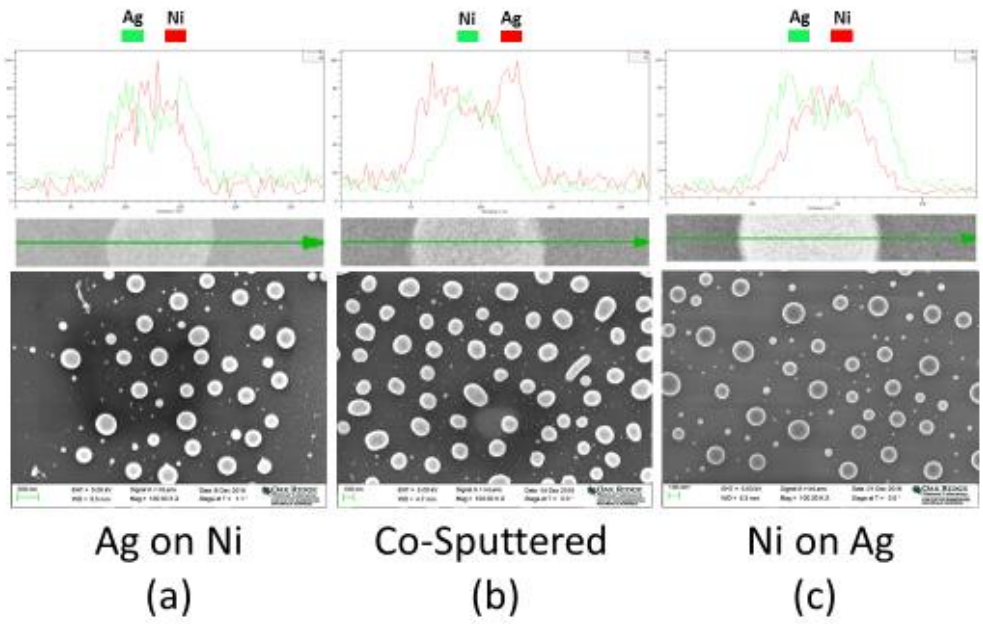

Figure 3. 2- SEM micrographs and EDX line scans of particles formed by the dewetting of co-sputtered, Ag on Ni, and Ni on Ag thin films. (a) 10 nm (at center) Ni thin film covered by 10nm (at center) Ag thin film, (b) 20 nm co sputtered Ni-Ag alloy thin film, and (c) 10 nm (at center) Ag thin film covered by a 10 nm (at center) Ni thin film.

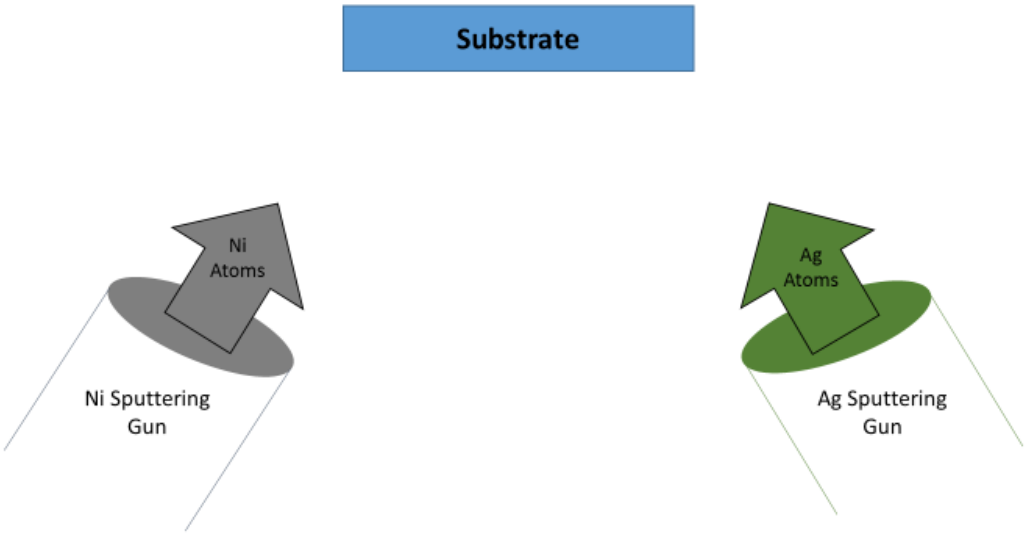

Figure 3. 3- Schematic featuring the sputtering set-up used to create a gradient during thin film deposition.

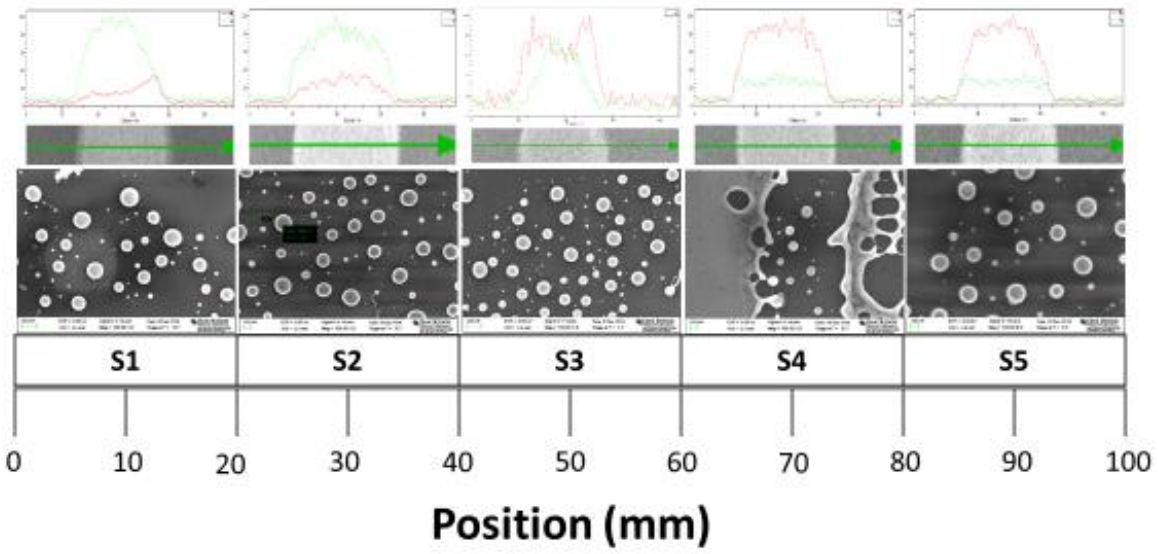

Figure 3. 4- SEM micrographs and EDX line scans of particles formed through dewetting of Ni-Ag co-sputtered thin films at different compositions. In the EDS line scans red is silver and green is nickel.

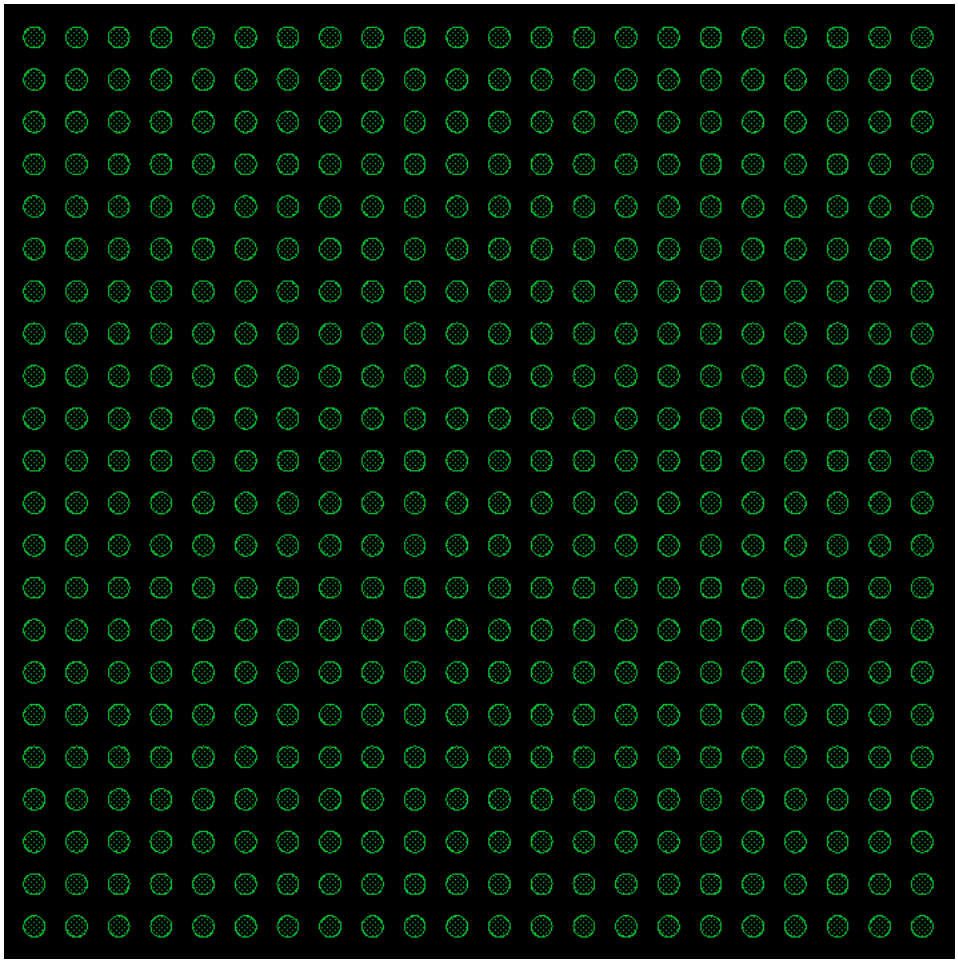

Figure 3. 5- 20x20 array of circles.

Figure 3.6 features circles increasing in diameter by 50 nm from 100 nm to 1 um with 200 nm spacing between each circle.

The increasing triangle pattern, featured in figure 3.7, has equilateral triangles increasing in side length by 25 nm from 100 nm to um with 200 nm spacing between each shape.

Figure 3.8, the increasing rectangle pattern, features rectangle with widths of 100 nm, 500 nm, 750 nm, and 1 um and lengths of 100 nm, 250 nm, 500 nm, 750 nm, and 1 um.

Figure 3.9 features a 3x3 array of ovals or "pills" that are made by putting a half circle with a diameter of 100 nm on opposite sides of a square with 100 nm side lengths.

Figure 3.10 consists of a triangular array of the oval pattern described above.

Figure 3.11, the square wave pattern, consists of a series of square waves with side lengths of 200 nm and 500 nm with spacing of 100 nm, 200 nm, 300 nm, 400 nm, and 500 nm.

Figure 3.12 features one mirrored triangular wave with triangles that have a 400 nm base and 600 nm height with 200 nm spacing between them and a series of triangles with a flat bottom that have an 800 nm base and 1.2 um height with 400 nm spacing between them.

The arcs and arrows pattern, featured in figure 3.13, consists of a series of arrows with 600 nm, 800 nm, and 1.2 um between each leg and heights of 1 um, 1.2 um, 1.6 um, and 1.8 um. It also features a quarter circle polygon arc with 200 nm side length, half circle polygon arc lengths with side lengths of 200 nm and 400 nm and inner diameters of 400 nm, 800 nm, and 1.2 um, and a three-quarter circle polygon arc with side lengths of 250 nm and an inner diameter of 400 nm.

The "bowtie" or "infinity" pattern, featured in figure 3.14, consists of 2 triangles made of three oval patterns (described above) mirroring each other.

Figure 3.15 consists various shapes and arrays featured in the unit pattern including different kinds of triangles, various arcs and hollowed circles, squares arranged in a circular shape, and circles arranged in a variety of ways.

The patterns described above were arrayed into a 250 um x 250 um square (featured in figure 3.16) and patterned onto our samples using the electron beam lithography (EBL) tool.

3.3 Patterned Film Dewetting on Bulk Substrates

After conducting the continuous thin film dewetting experiments on bulk substrates we decided to explore the effects on particle formation by patterning films using the shapes and arrays described above. By first patterning a film then performing pulsed laser induced dewetting, it is possible to create arrays with controllable size, composition, and symmetry.

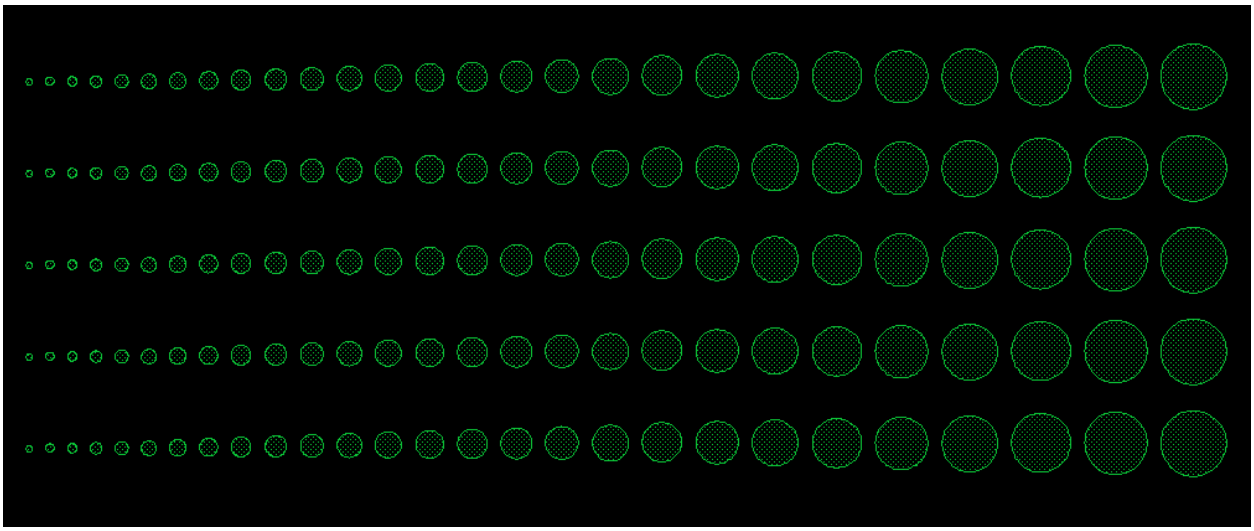

Figure 3. 6- Increasing circle pattern.

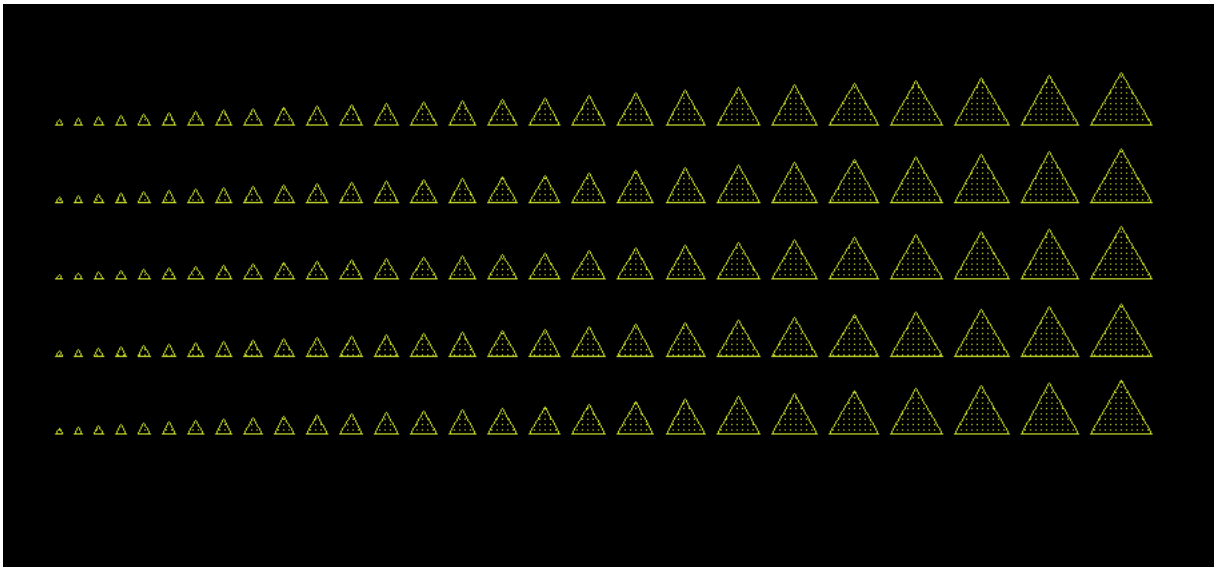

Figure 3. 7- Increasing Triangle Pattern.

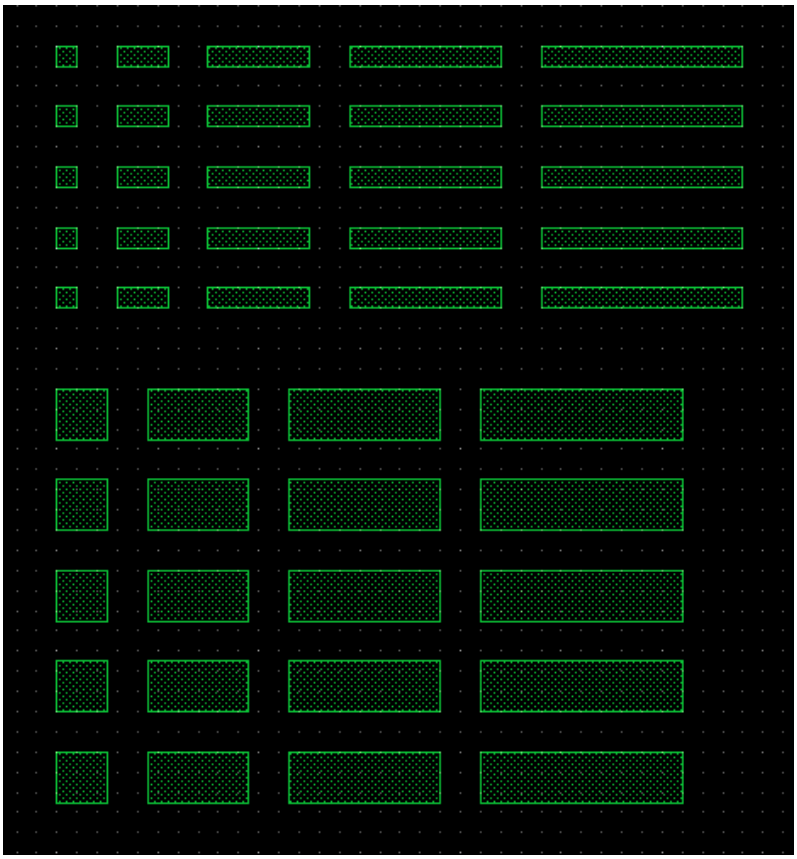

Figure 3. 8- Increasing rectangle pattern.

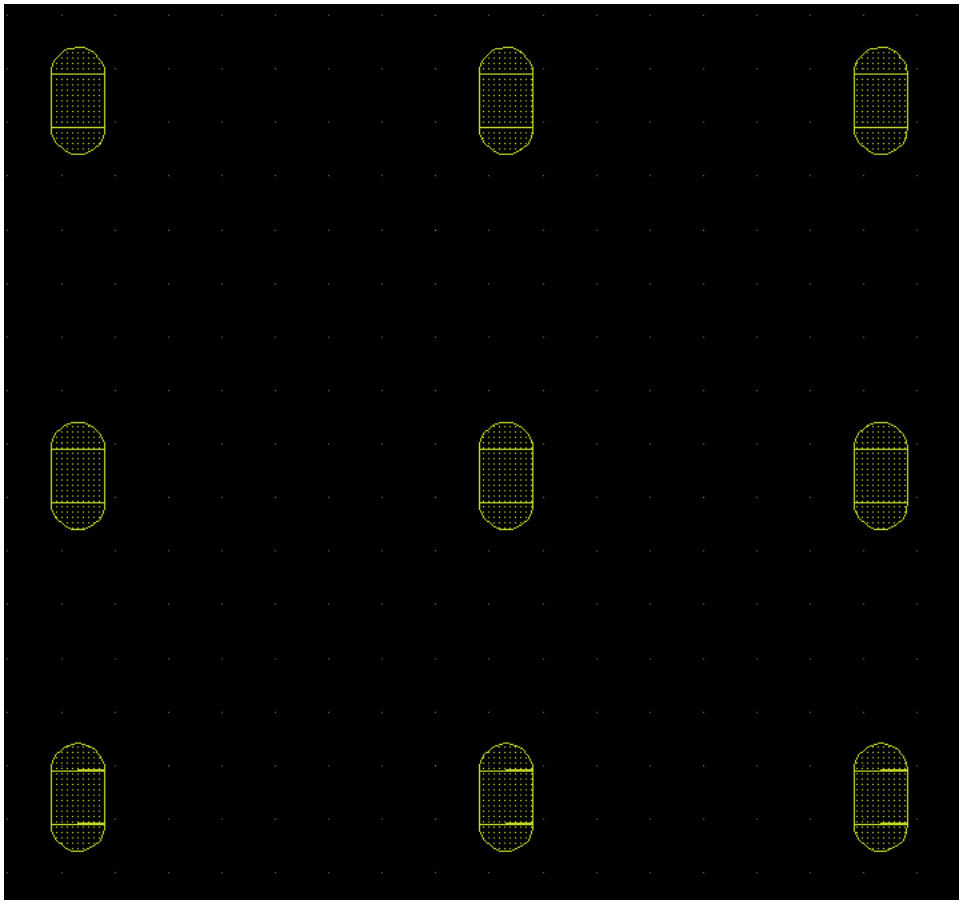

Figure 3. 9- Array of ovals or “pill” pattern.

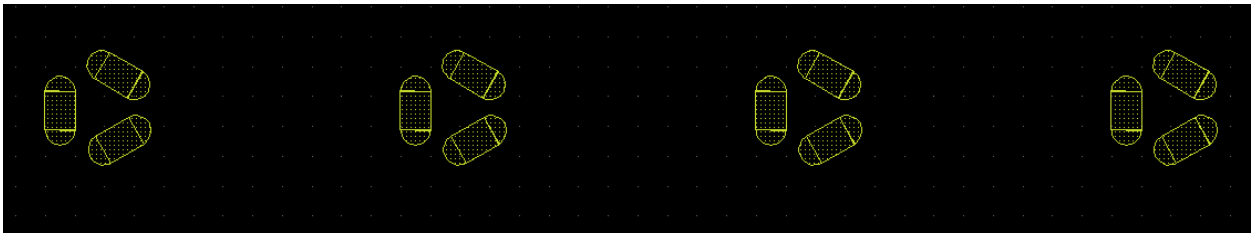

Figure 3. 10- Triangular array of oval patterns.

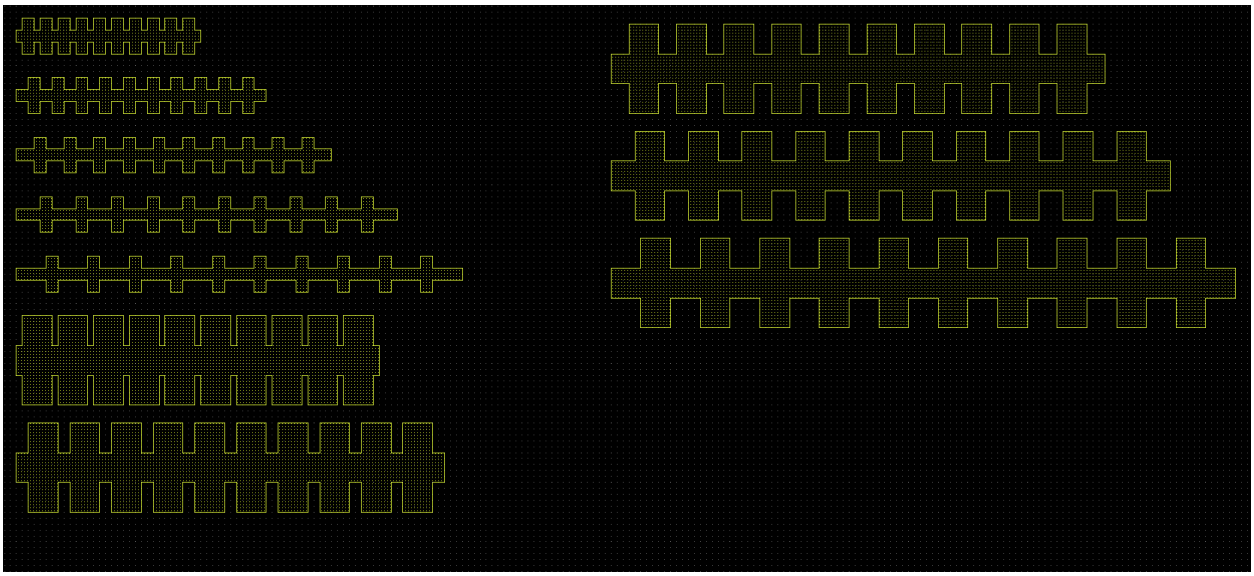

Figure 3. 11- Square wave pattern.

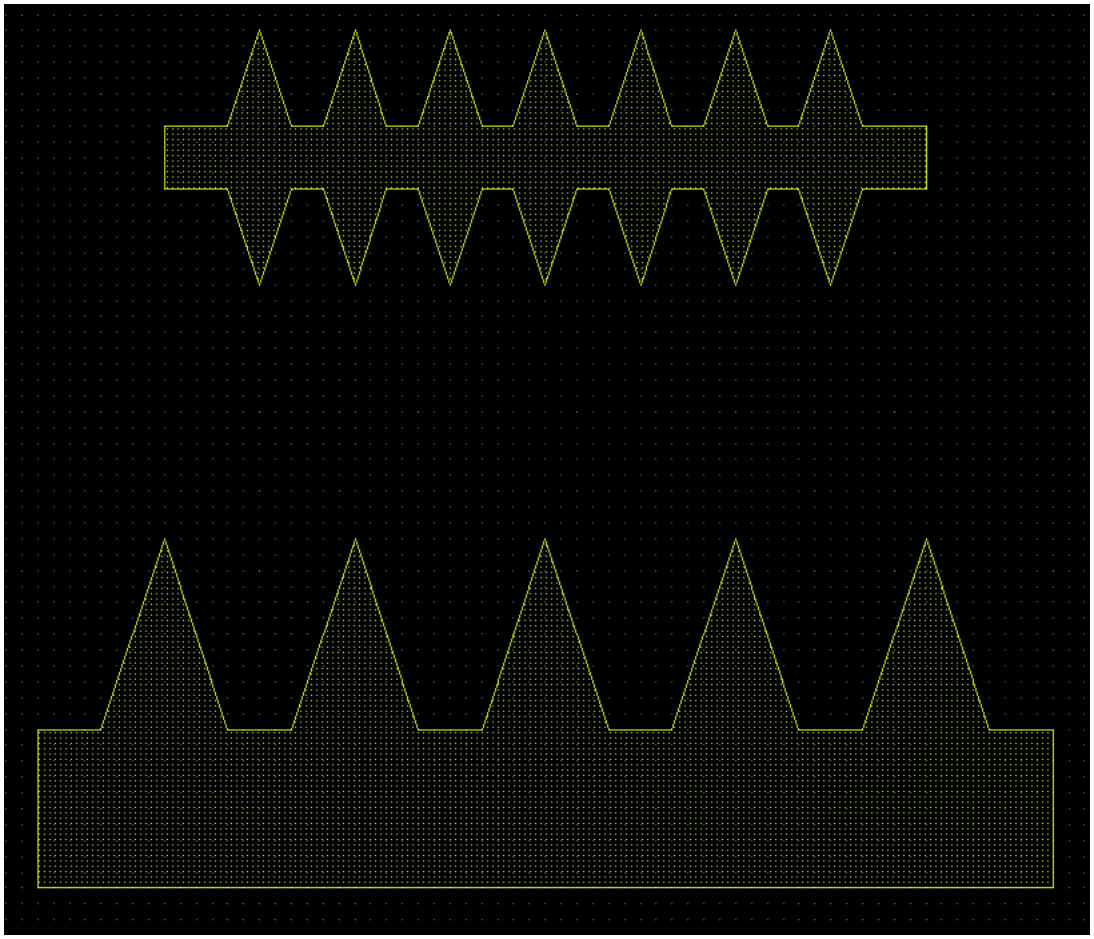

Figure 3. 12- Triangular wave pattern.

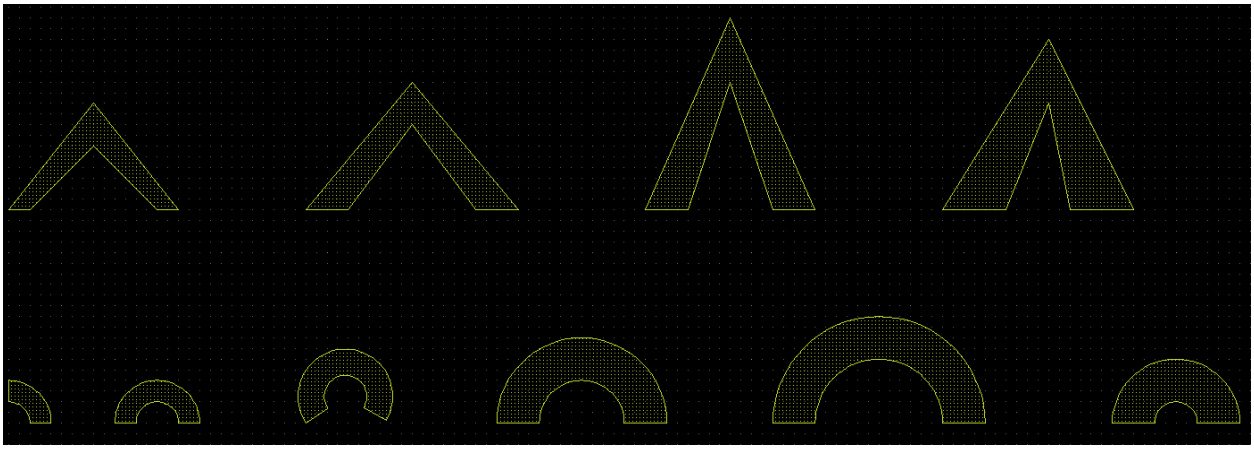

Figure 3. 13- Arcs and arrows pattern.

Figure 3. 14- “Bowtie” or “Infinity” Pattern.

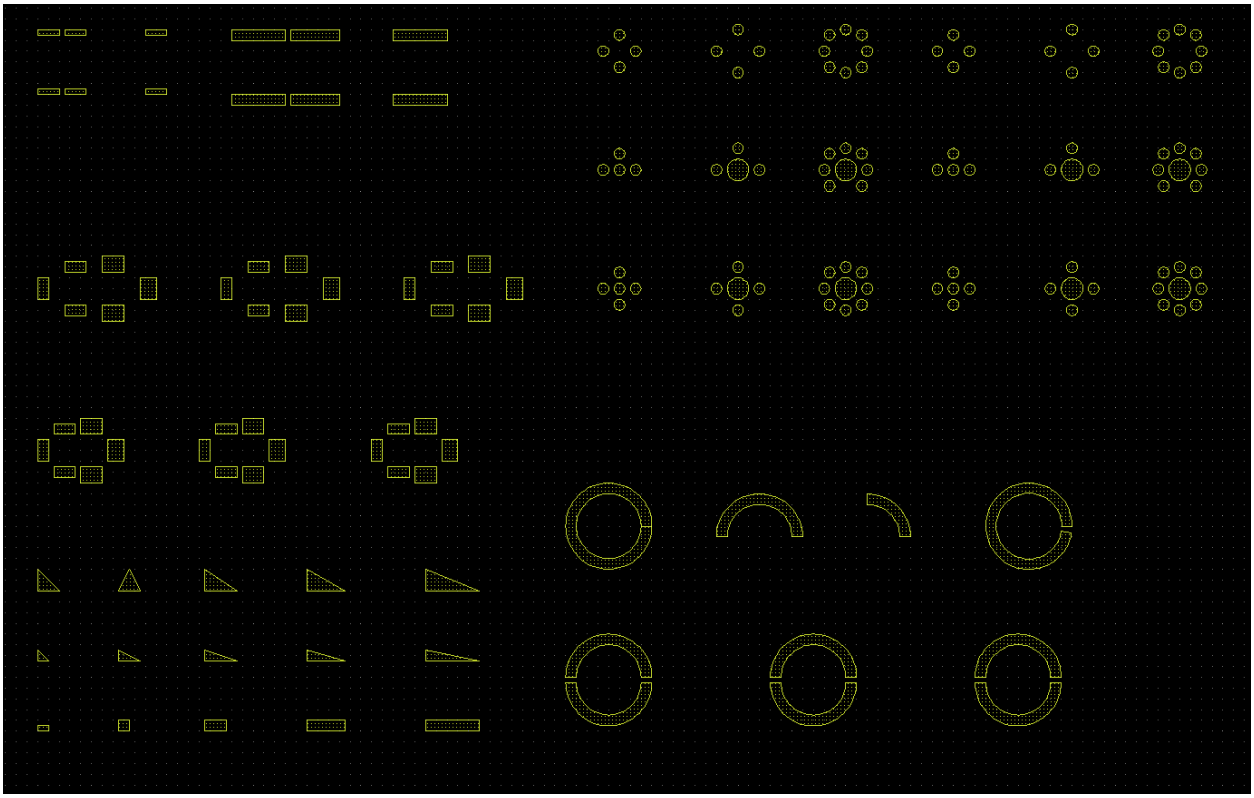

Figure 3. 15- Various other shapes and arrays included in the unit pattern.

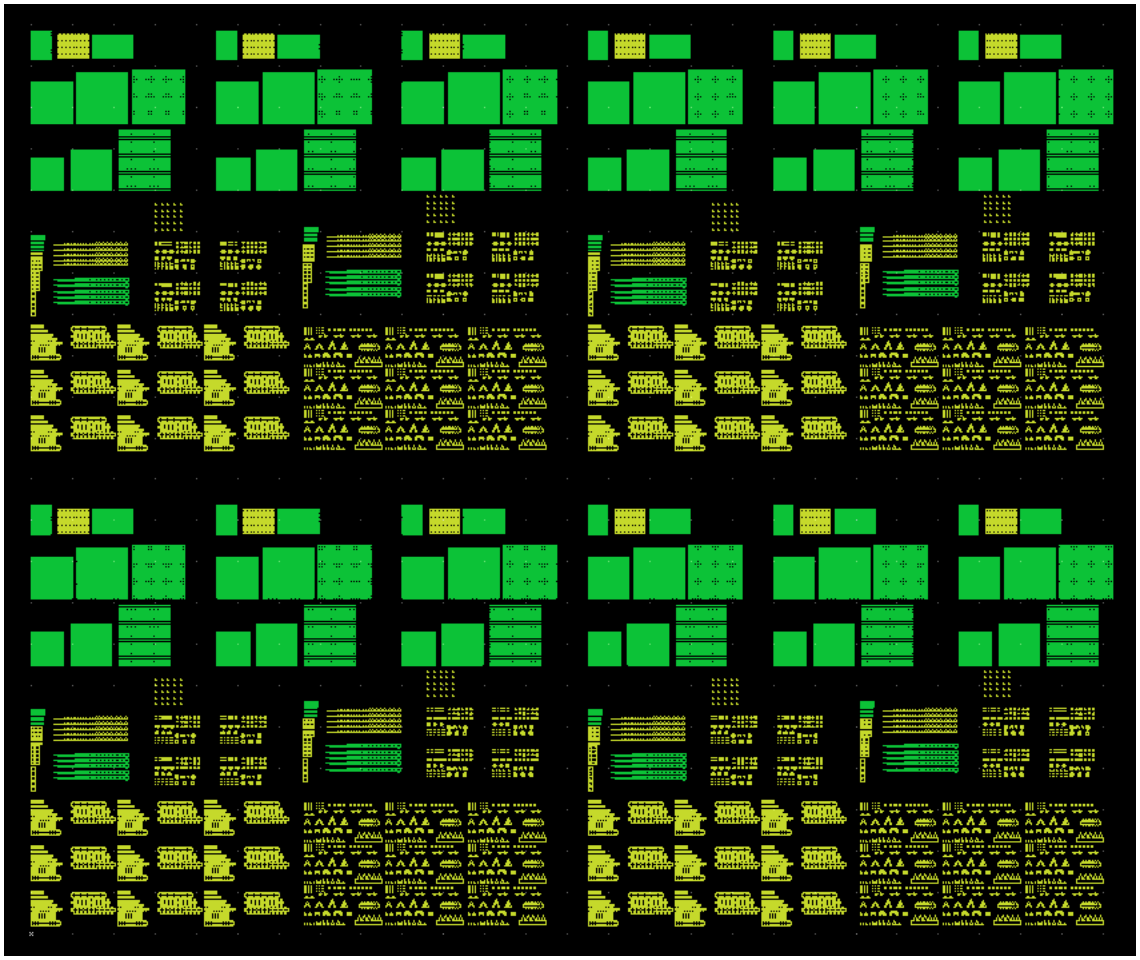

Figure 3. 16- Full view of the unit pattern.

3.3.1 Nickel Top Silver Bottom Bottom-Layer Patterning

Nickel top Silver bottom bottom-layer patterning describes a technique in which the bottom layer, silver, is patterned using the arrays and shapes described above. These patterns are then covered with a continuous nickel film and exposed to laser irradiation. We fabricated multiple samples on a silicon substrate coated with 100 nm SiO_2 by patterning a photoresist layer using the EBL, depositing 10 nm of silver on the exposed photoresist, lifting off using acetone, then depositing a continuous 10 nm thin film of nickel on top. Figure 3.17 features a schematic of the sample described above and figure 3.18 features a summary of our results.

The SEM micrographs above showcase the difficulties of the nickel top sample assembly. Nickel has a much higher melting temperature than silver and thus takes a higher laser energy to induce melting and dewetting. Although there is particle formation, they are not highly ordered like we hope to achieve through these experiments. The particles form at the location of the patterned circles and there are rivulet connections between them. Nickel is also very hard to liftoff which makes fabricating these types of samples more difficult.

3.3.2 Silver Top Nickel Bottom Bottom-Layer Patterning

Silver top nickel bottom bottom-layer patterning describes the same fabrication technique as above, but with a reversal of the metallic depositions. These samples were fabricated on a silicon substrate coated with 100 nm SiO_2 by patterning a photoresist layer using the EBL, depositing 10 nm of nickel on the exposed photoresist, lifting off using acetone, then depositing a continuous 10 nm thin film of silver on top. Figure 3.19 features a schematic of the sample described above and figures 3.20 and 3.21 features a summary of our results.

These SEM micrographs show two different and very interesting results for the silver top nickel bottom bottom-layer pattern. Figure 3.20 features a fully dewetted circular array pattern in which a repeated array of primary, secondary, tertiary, and quaternary particles are formed. The primary particles form where the circles were originally patterned. The secondary particles form at interstitial points in between 4 primary particles and the tertiary and quaternary particles form on either side of the primary particle. Figure 3.21 showcases the large difference in melting temperatures between nickel and silver. The laser energy was high enough to cause the silver to melt, but not the nickel and thus the silver particles form on top of the original nickel patterns.

3.3.3 Silver Top Nickel Bottom Top-Layer Patterning

Silver top nickel bottom top-layer patterning describes a fabrication method very similar to the bottom-layer patterning described above, except the second metal is patterned on top of a

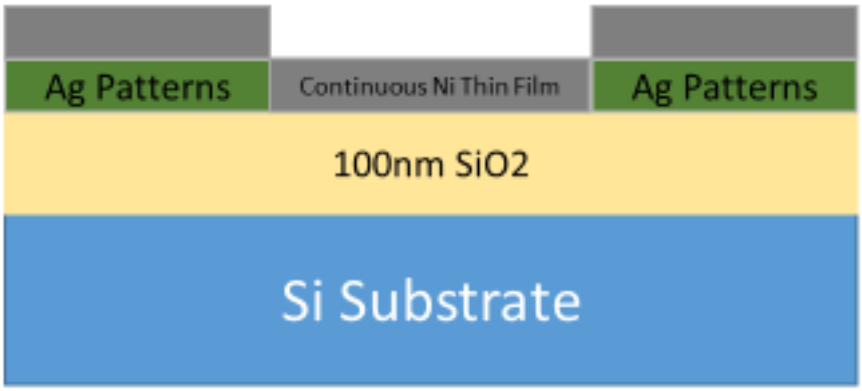

Figure 3. 17- Schematic featuring the nickel top silver bottom bottom-layer pattern.

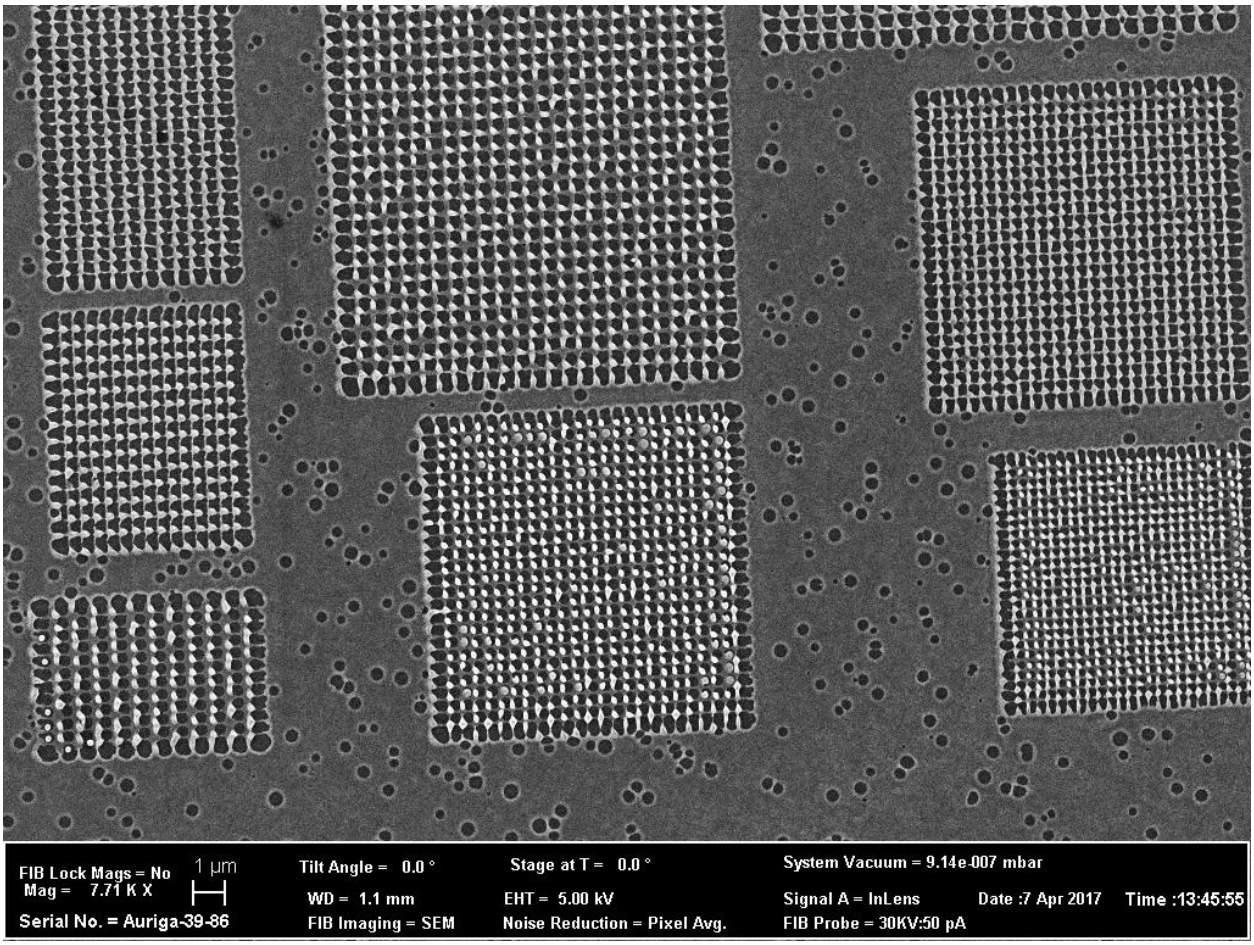

Figure 3. 18- SEM micrograph of the nickel top silver bottom bottom-layer pattern after laser treatment.

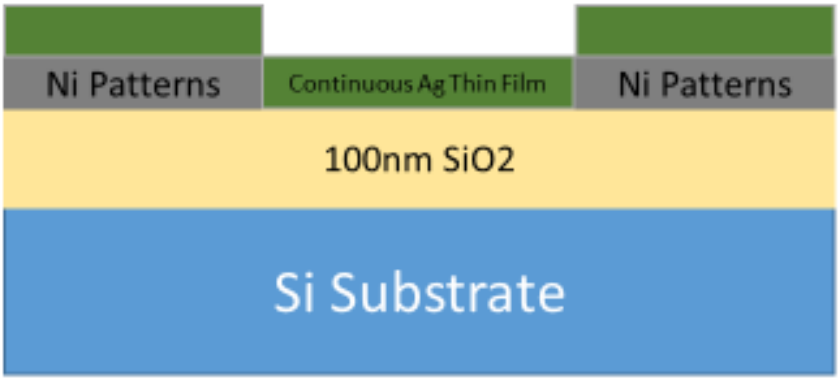

Figure 3. 19- Schematic featuring the silver top nickel bottom bottom-layer pattern.

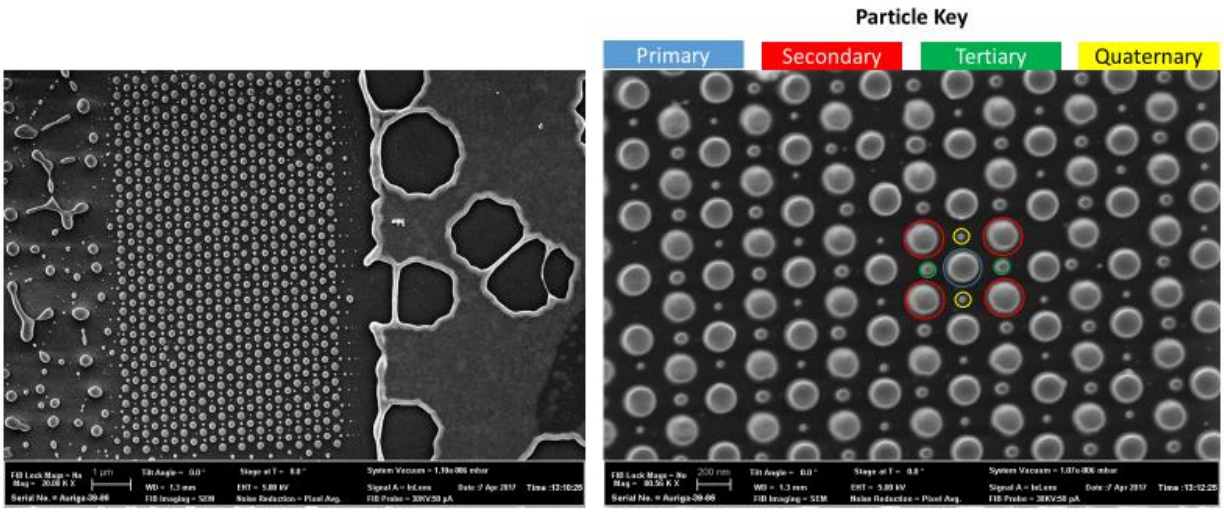

Figure 3. 20- SEM micrographs of fully dewetted silver top nickel bottom bottom-layer patterns.

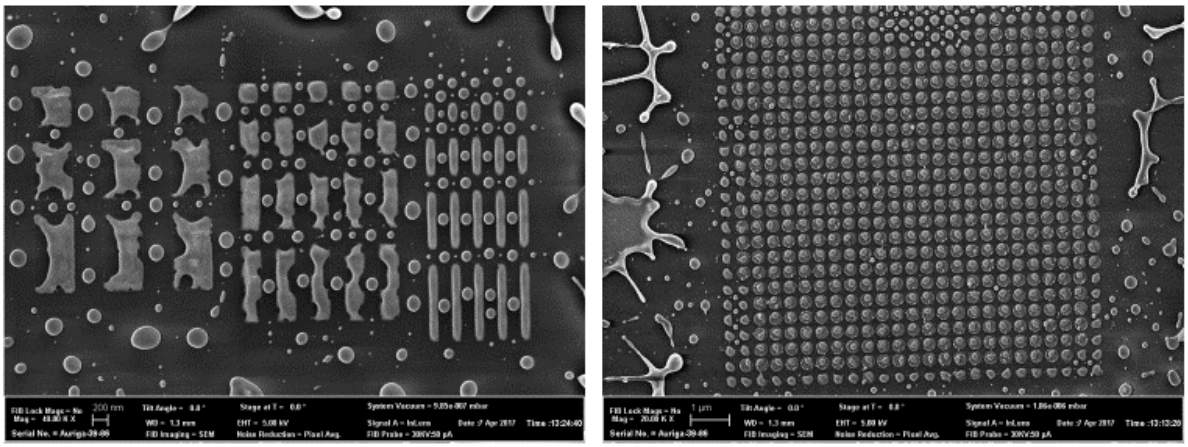

Figure 3. 21- SEM micrographs of partially dewetted silver top nickel bottom bottom-layer patterns.

continuous thin film of the first metal. These samples were fabricated on a silicon substrate coated with 100 nm SiO_2 by depositing 10 nm of nickel on the SiO_2 layer, spin coating a layer of photoresist on top of the nickel, patterning the photoresist using the EBL, then depositing 10 nm of silver on top of the exposed photoresist and finally lifting off using acetone. Figure 3.22 features a schematic of the sample described above and figure 3.23 features a summary of our results.

The SEM micrographs show some patterned particle formation, but not nearly as much as the silver top nickel bottom bottom-layer pattern. The EDX scans show the consequences of trying to form particles with metals that have such different melting temperatures. There is absolutely no trace of silver in these scans, meaning that the laser completely ablated all silver from the film, leaving only nickel particles. Interestingly, the top silver layer clearly impacts the pattern formation, but is subsequently evaporated.

3.3.4 Nickel Top Silver Bottom Top-Layer Patterning

Nickel top silver bottom top-layer patterning describes the same method as above, except the silver is deposited first as the continuous film and the nickel is patterned on top. Figure 3.24 features a schematic of the sample described above. No SEM micrographs of this sample were captured because complete ablation or island growth of the patterned silver film was the only dewetting observed.

3.4 Patterned Film Dewetting on TEM Membranes

One of the ultimate goals of this study is to prepare for the arrival of a laser system attachment for the TEM which will be capable of heating and photoexcitation allowing us to conduct *in situ* TEM dewetting experiments. In order to do this, we have attempted to conduct the experiments described above on TEM membrane instead of bulk substrates. This is very difficult as the windows on the TEM membranes are typically on the order of only 30 nm thick and are therefore very fragile. We also must tune the laser energy which is necessarily much lower due to minimal heat dissipation via thermal conduction in the thin membranes and must not be too excessive to avoid annihilation of the TEM windows during laser treatment. Figure 3.25 features an SEM micrograph of a broken membrane window.

Another problem we have faced is during the lift-off portion of our fabrication method. Since we are using wet lift-off, it requires us to submerge the membrane in acetone which is typically done under sonication; this however is a very violent process for the fragile TEM membrane windows. It is very difficult not to break the windows during liftoff and thus we have had difficulties fabricating patterned TEM membranes.

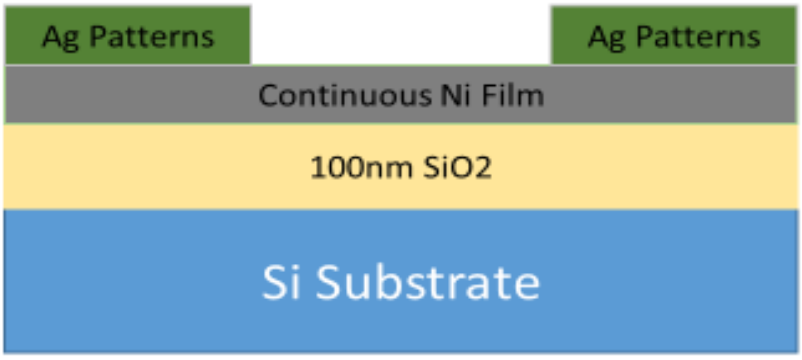

Figure 3. 22- Schematic featuring silver top nickel bottom top-layer pattern.

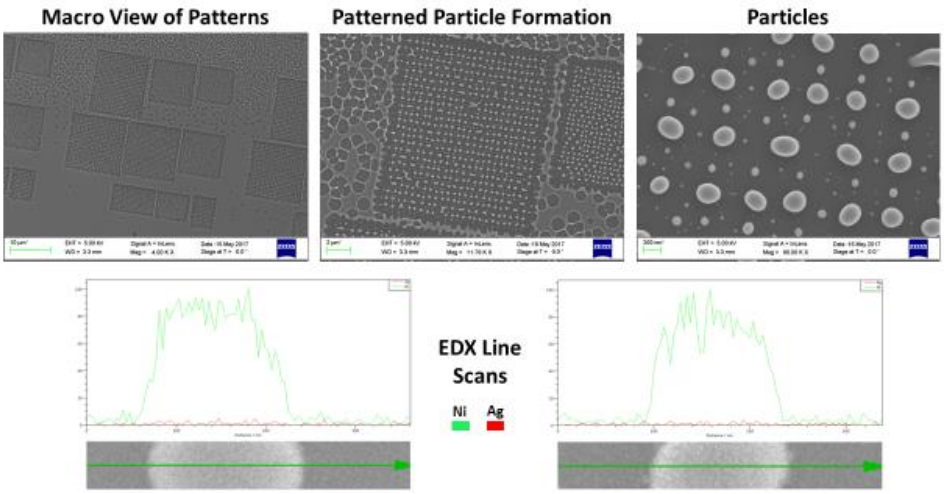

Figure 3. 23- SEM micrographs and EDX line scans of particles formed by pulsed laser induced dewetting of the silver top nickel bottom top-layer pattern.

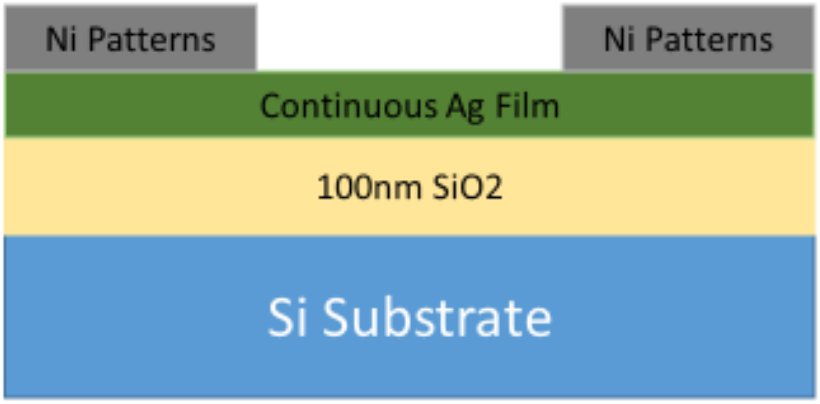

Figure 3. 24- Schematic featuring the nickel top silver bottom top layer pattern.

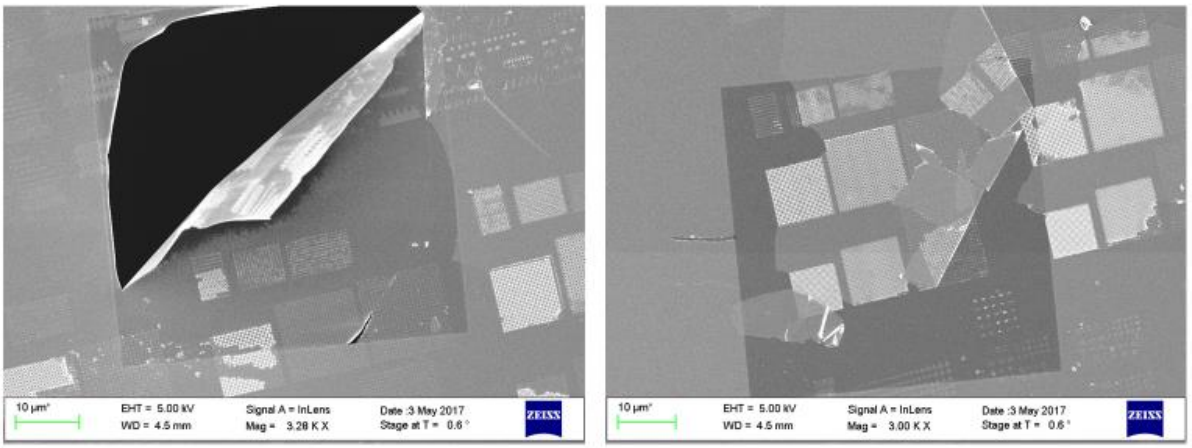

Figure 3. 25- SEM micrographs of broken TEM membranes. (a) SEM micrograph of a TEM membrane tearing due to laser annihilation. (b) SEM micrograph showing photoresist persisting on the membrane window.

3.4.1 Silver Top Nickel Bottom Bottom-Layer Patterning

The fabrication method for these samples is the same as in the section described above except the patterns are synthesized directly onto the TEM windows. Figure 3.26 features a summary of our results.

Figure 3.26 also overviews the fabrication process. The as deposited SEM micrographs show patterned nickel with a continuous silver film on top on the membrane windows. As with prior samples, the post laser treatment images show only partial dewetting; due to the disparate melting temperatures, the silver melts and transforms into particles but the nickel does not melt and remains as-patterned. The EDX line scans demonstrate this point as they show nickel on the outside and silver on the inside of the scan.

3.5 Ni-Ag Co-Sputtered Compositional Progression Study on TEM Membrane

In this study, we explored the effects on particle formation by varying the ratios of silver and nickel on each sample (similar to section 3.1.3, except this time on TEM membranes). To do this, we simultaneously sputtered 10 nm of nickel and 10 nm of silver on 30 nm SiN_x TEM membrane windows. The sputtering guns were parallel to each end of the sample and thus formed a gradient (See figure 3.3 for clarification). Our substrate was roughly 10cm in length and after the thin film deposition was broken into five 2 cm pieces that we refer to as: S1 (roughly 90% Ag and 10% Ni), S2 (roughly 70% Ag and 30% Ni), S3 (roughly 50% Ag and 50% Ni), S4 (roughly 30% Ag and 70% Ni), and S5 (roughly 10% Ag and 90% Ni) (refer to Figure 2.1-(d) for clarification). A summary of our results is featured in Figure 3.27.

These STEM images were taken in bright field mode so the appearance of brighter areas in the particles are representative of silver and the darker areas show nickel. The STEM images gave very interesting results, showing a very low Ni composition in the particles on S1, a slightly higher composition of Ni in the particles on S2, half-half particle formation and almost equal counts of Ag and Ni on S3, a very low composition of Ag in the particles on S4, and only a slight trace of Ag in the particles on S5. We are in the process of acquiring TEM images on these samples to better understand the particle structure and morphology.

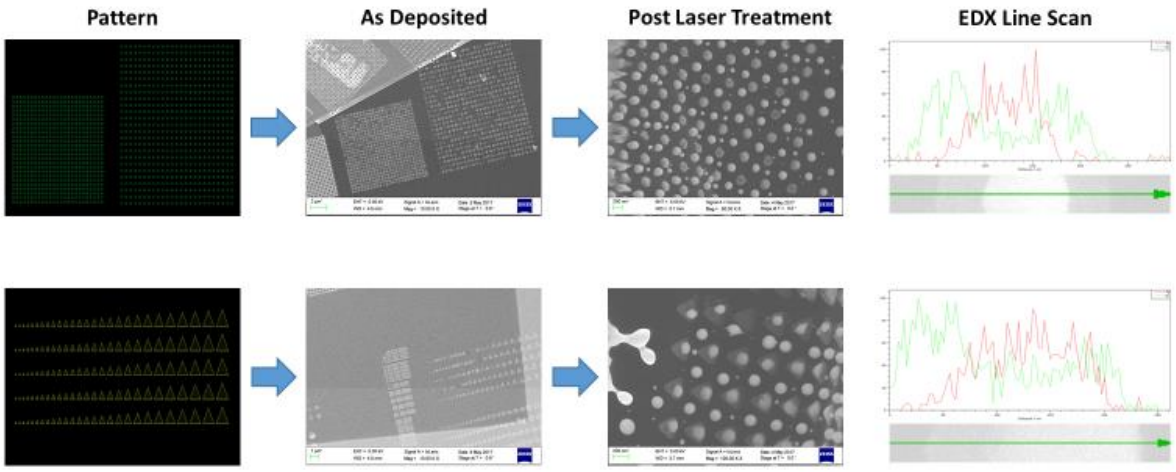

Figure 3. 26- Layout Editor patterns, as-deposited SEM micrographs, post laser treated micrographs, and EDX line scans of the silver top nickel bottom bottom-layer patterning method on TEM membranes.

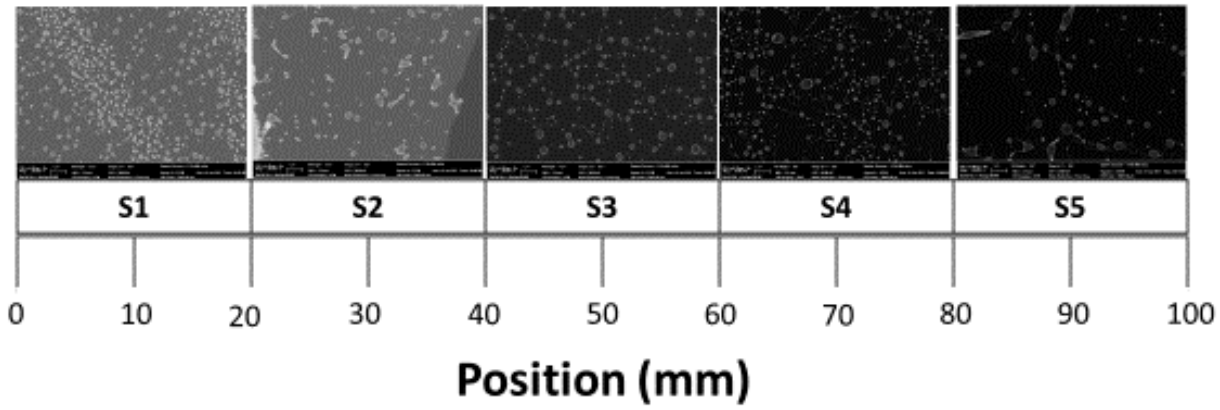

Figure 3. 27- Scanning transmission electron micrographs (STEM) of particles formed through dewetting of Ni-Ag co-sputtered thin films at different compositions on TEM membranes.

Chapter 4 Discussion

4.1 Nano-particle formation: Half-Half Vs. Core-Shell

The above experiments conducted using the Ni-Ag system revealed that both core-shell and half-half particles can be formed through pulsed laser induced dewetting (see figure 4.1 for a schematic of both particle types). Core-shell particles formed on bulk substrates while half-half particles only formed on TEM membrane windows. This can be explained by analyzing the equilibrium and non-equilibrium solidification methods present in the different substrates. The large thickness of the bulk substrates causes a rapid heat sink after laser irradiation and therefore decreases the liquid lifetime of the metallic thin film while the roughly 30 nm SiN_x TEM membrane windows do not allow for such a rapid heat sink and therefore stay at a much higher temperature for an extended period of time leading to a very long liquid lifetime. The reasoning behind these conclusions will be further explained in the following sections.

4.1.1 Equilibrium and non-equilibrium solidification

When the cooling rate is extremely slow, as is the case for thin film dewetting on TEM membrane windows, equilibrium solidification occurs and a homogeneous solid phase is formed resulting in half-half nano-particle formation. When the cooling rate and thus solidification occurs at a faster rate, which happens during thin film dewetting on bulk substrates, diffusion is insufficient to homogenize the metallic composition and thus non-equilibrium solidification occurs which results in core-shell nano-particles.

4.1.2 Core solidification of the Ag-Ni system

The Ni atomic composition in the 50/50 films is ~50% and is labeled by the blue line in figure 4.2. The 50/50 thin films on bulk substrates rapidly melt into their liquid phases after laser irradiation and rapidly cool due to the large heat sink on bulk substrates. Based on the phase diagram, it is clear that as the temperature decreases, Ni begins to solidify first because it has a higher melting temperature (labeled T1). This fast, non-equilibrium cooling causes a solid Ni core to be surrounded by a liquid Ag matrix. Upon further cooling to temperature T2, the outer liquid Ag matrix begins to solidify to form the shell of the core-shell particle featured in figure 4.1.

However, if the cooling rate is slow as is the case with 50/50 films on TEM membranes, equilibrium cooling is dominate and allows for the formation of the half-half nano-particle type

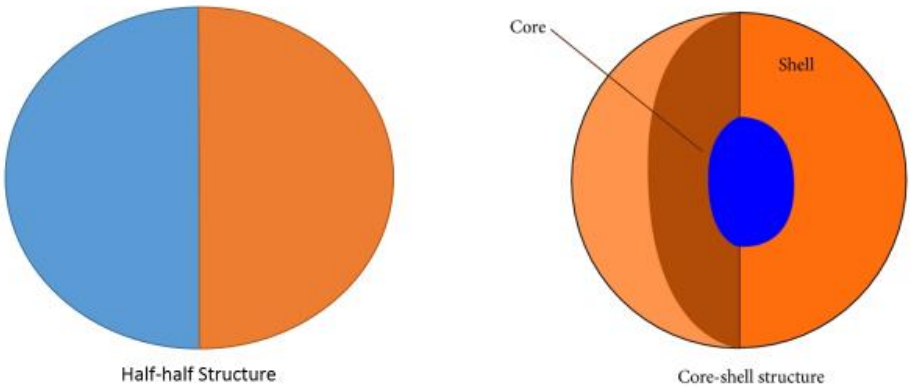

Figure 4. 1- Schematics featuring the half-half and core-shell nano-particle structure.

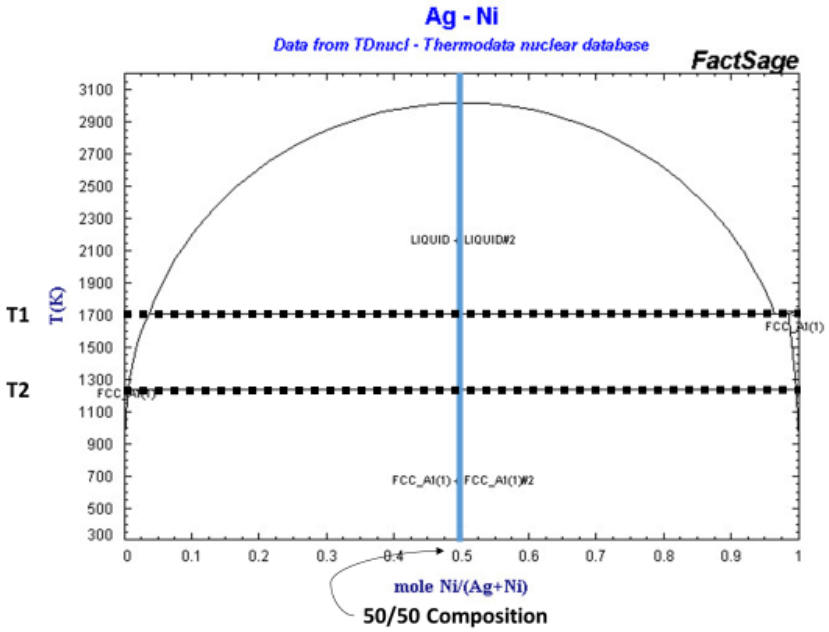

Figure 4. 2- Phase diagram of Ag-Ni binary system.

featured in figure 4.1. The Ni-Ag system forms half-half particles instead of a particle consisting of a uniform mixture of the two metals because Ni and Ag are immiscible.

4.2 Diffusion in Ag-Ni nano-particles

The core-shell particle morphology is a stable intermediate phase as it minimizes the strain due to the large lattice mismatch between Ni and Ag atoms [53-55]. However, as Malviya et al. showed in the silver-copper system, continued heating of the bi-metallic nano-particles leads to a half-half morphology. The continued heating present on the TEM membrane windows due to the lack of heat diffusion causes recrystallization of the particles as well as the Ag-rich phase to nucleate to the surface of the particle. The Ag-rich phase nucleates to the outside of the particle because it is more stable than Ni as it has a lower surface energy (Ag has a surface energy of .925 $\frac{J}{M^2}$ and Ni has a surface energy of 1.781 $\frac{J}{M^2}$). As the heating continues, the core-shell particle will continue to undergo diffusion-induced phase separation and growth during recrystallization which will eventually lead to the half-half particle morphology [57]. Figure 4.3 features a schematic of this process.

4.3 Using interfacial tensions to predict particle morphology

The Gibbs free energy change for structural development of a particle during formation can be described using a combination of enthalpic, entropic, and surface free energy terms. The enthalpic change can be ignored when the analysis is done for different shaped particles in the same stage of the reaction process and because the particles are much larger than the individual molecules they are made of, the differences in entropic free energy between different particle types can also be ignored. Thus, the Gibbs free energy change can be written as

$$\Delta G = \sum_i \gamma_i A_i, \tag{4.1}$$

Where γ_i is the interfacial tension at surface "i" and A is the area of the interface. This definition can be expanded to specific particle morphologies and thus we did so to evaluate the plausibility of each particle morphology type. The Free energy change associated with core-shell particle formation can be described using:

$$\Delta G_{CS} = \gamma_{M_c-M_s} * A_{M_C-M_S} + \gamma_{M_S-Air} * A_{M_s-Air} + \gamma_{M_c-Sub} * A_{M_c-Sub} + \gamma_{M_s-Sub} * A_{M_S-Sub} \tag{4.2}$$

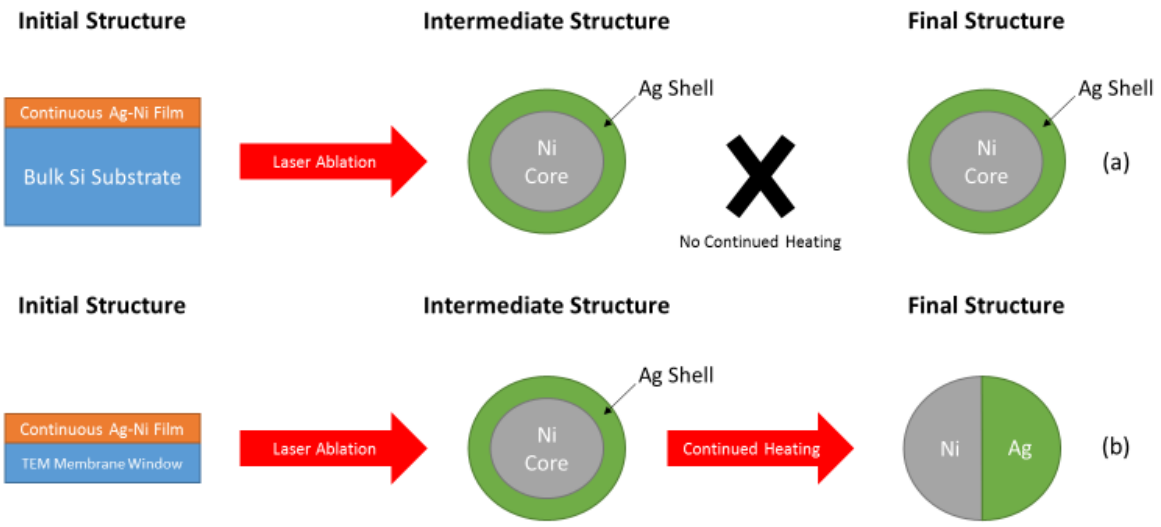

Figure 4. 3- Schematic showing the evolution in particle morphology due to heat dissipation difference in (a) bulk substrates and (b) TEM Membranes.

Where $\gamma_{M_c-M_s}$ is the interfacial tension between the core metal and shell metal, $A_{M_C-M_S}$ is the area of the core metal and shell metal interface, γ_{M_S-Air} is the interfacial tension between the surface metal and the air, γ_{M_c-Sub} is the interfacial tension between the core metal and the substrate, A_{M_c-Sub} is the area of the core and substrate interface, γ_{M_s-Sub} is the interfacial tension between the shell metal and the substrate, and A_{M_S-Sub} is the area of the shell metal and substrate interface. This equation was adapted to our situation from an equation originally intended to predict the particle morphology of two immiscible polymers submerged in a liquid medium [59]. For our calculations, Nickel is the core metal and silver is the shell metal. The free energy change associated with half-half particle formation can be described by:

$$\Delta G_{HH} = \gamma_{M_1-M_2} * A_{M_1-M_2} + \gamma_{M_1-M_{Air}} * A_{M_1-M_{Air}} + \gamma_{M_2-M_{Air}} * A_{M_2-M_{Air}} + \gamma_{M_1-M_{Sub}} * A_{M_1-M_{Sub}} + \gamma_{M_2-M_{Sub}} * A_{M_2-M_{Sub}}, \quad (4.3)$$

Where $\gamma_{M_1-M_2}$ is the interfacial tension between the two metals in the particle, $A_{M_1-M_2}$ is the area of the interface between the two metals in the particle, and the rest of the terms in the equation have been defined above. For our calculations, nickel is metal 1 and silver is metal 2. In order to calculate the Gibbs free energy change during core-shell and half-half particle formation it was assumed that in both cases the particle had a 50 nm radius, hemispheres or a half particle actually formed on the surface (see figure 4.4), and equal volumes of both metals were present. The interfacial tension between liquid silver and liquid nickel is unknown and therefore our model includes a low ($.3\frac{J}{m^2}$), medium ($1\frac{J}{m^2}$), and high ($2\frac{J}{m^2}$) energy case to see how each would affect the energetics of particle formation. ΔG_{CS} (low), ΔG_{CS} (medium), and ΔG_{CS}(high) represent the Gibbs free energy change during formation of core-shell particles with low, medium, and high silver-nickel interaction energies and ΔG_{HH}(low), ΔG_{HH}(medium), ΔG_{HH}(high) represent the Gibbs free energy change during formation of half-half particles with low, medium, and high silver-nickel interaction energies. The values in tables 4.1 and 4.2 were used in the calculation of the Gibbs free energy change during core-shell and half-half particle formation[56, 58,60]:

According to our analysis, the core-shell morphology will preferentially form in the low and medium silver-nickel interface energy cases and the half-half morphology is preferred in the high nickel-silver interaction energy case. This is because the silver-nickel interaction area in the core-shell particle morphology is much larger than the half-half morphology and thus more energy is required as the interaction energy increases. We believe that both surface interaction dynamics and solid state diffusion caused by the continued heating on TEM membrane windows lead to the half-half particle morphology.

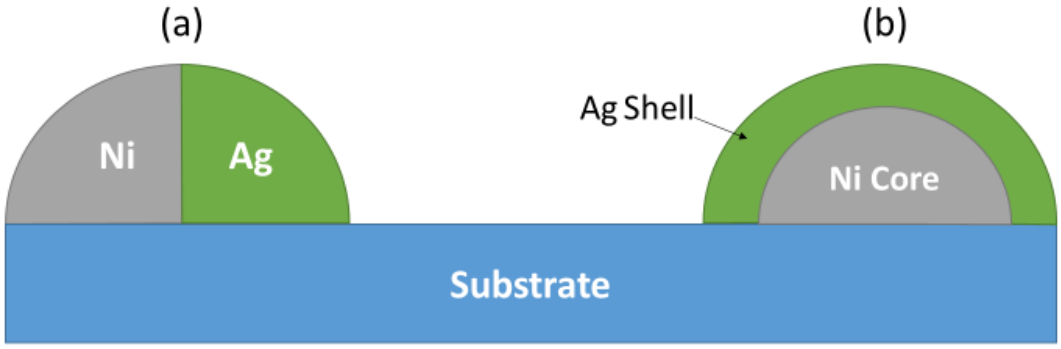

Figure 4. 4- Schematic featuring a vertical cut of different particle morphologies used to model Gibbs free energy of formation. (a) features a half-half particle and (b) features a core-shell particle.

Table 4. 1- Values for the terms in equation 4.2 (core-shell particle formation).

Term	Ag-Ni System Value
$\gamma_{M_c-M_s}$ (low, medium, high)	.3, 1, 2 $\frac{J}{m^2}$
$A_{M_C-M_S}$	9.895 E-15 m^2
γ_{M_S-Air}	.925 $\frac{J}{m^2}$
A_{M_S-Air}	1.571E-14 m^2
γ_{M_c-Sub}	.414 $\frac{J}{m^2}$
A_{M_c-Sub}	4.947 E-15 m^2
γ_{M_s-Sub}	1.405 $\frac{J}{m^2}$
A_{M_S-Sub}	2.906E-15 m^2
ΔG_{CS} (low)	**2.362 E-14 J**
ΔG_{CS} (medium)	**3.055 E-14 J**
ΔG_{CS} (high)	**4.044 E-14 J**

Table 4. 2- Values for terms in equation 4.3 (half-half particle formation).

Term	Ag-Ni System Value
$\gamma_{M_1-M_2}$(low, medium, high)	.3, 1, 2 $\frac{J}{m^2}$
$A_{M_1-M_2}$	3.926 E-15 m^2
γ_{M_1-Air}	1.781 $\frac{J}{m^2}$
A_{M_1-Air}	7.853 E-15 m^2
$\gamma_{M_2-M_{Air}}$	.925 $\frac{J}{m^2}$
$A_{M_2-M_{Air}}$	7.853 E-15 m^2
$\gamma_{M_1-M_{Sub}}$	.414 $\frac{J}{m^2}$
$A_{M_1-M_{Sub}}$	3.926 E-15 m^2
$\gamma_{M_2-M_{Sub}}$	1.405 $\frac{J}{m^2}$
$A_{M_2-M_{Sub}}$	3.926 E-15 m^2
ΔG_{HH} (low)	**2.956 E-14 J**
ΔG_{HH} (medium)	**3.232 E-14 J**
ΔG_{HH} (high)	**3.624 E-14 J**

Chapter 5 Conclusions

Ni-Ag alloy nano-particles were fabricated via pulsed laser induced dewetting on both patterned and continuous thin films. The nano-particle distribution, nano-particle type, and resulting nano-particle pattern were studied as a function of film structure, initial film pattern, and elemental composition.

We observed core-shell nano-particle formation on bulk substrates at 50/50 composition regardless of the order of thin-film deposition. This can be explained through non-equilibrium cooling and by observing the phase diagram.

These experiments demonstrated that both core-shell and half-half Ni-Ag nano-particles can be formed by simply tuning the substrate.

Ni-Ag thin films can be structured and patterned to form consistent networks of Ni-Ag nano-particles on both bulk and TEM membrane substrates. Therefore, it is possible to tune the dewetting process to achieve directed assembly of nano-particle arrays.

References

[1] B. A. Parviz, D. Ryan, and G. M. Whitesides, “Using self-assembly for the fabrication of nano-scale electronic and photonic devices,” *IEEE Trans. Adv. Packag.*, vol. 26, no. 3, pp. 233–241, Aug. 2003.
[2] J. B. Edel, A. A. Kornyshev, A. R. Kucernak, and M. Urbakh, “Fundamentals and applications of self-assembled plasmonic nanoparticles at interfaces,” *Chem. Soc. Rev.*, vol. 45, no. 6, pp. 1581–1596, 2016.
[3] M. Heiss *et al.*, “Self-assembled quantum dots in a nanowire system for quantum photonics,” *Nat. Mater.*, vol. 12, no. 5, pp. 439–444, May 2013.
[4] G. M. Whitesides, J. K. Kriebel, and B. T. Mayers, “Self-Assembly and Nanostructured Materials,” in *Nanoscale Assembly*, W. T. S. Huck, Ed. Springer US, 2005, pp. 217–239.
[5] J. Bischof, D. Scherer, S. Herminghaus, and P. Leiderer, “Dewetting modes of thin metallic films: Nucleation of holes and spinodal dewetting,” *Phys. Rev. Lett.*, vol. 77, no. 8, pp. 1536–1539, Aug. 1996.
[6] X. Li, Y. He, Y. Wang, J. Dong, and H. Li, “Dewetting Properties of Metallic Liquid Film on Nanopillared Graphene,” *Sci. Rep.*, vol. 4, p. 3938, Feb. 2014.
[7] J. Polte, “Fundamental growth principles of colloidal metal nanoparticles – a new perspective,” *CrystEngComm*, vol. 17, no. 36, pp. 6809–6830, 2015.
[8] R. P. Sear, “Nucleation: theory and applications to protein solutions and colloidal suspensions,” *J. Phys. Condens. Matter*, vol. 19, no. 3, p. 033101, 2007.
[9] C. Redon, F. Brochardwyart, and F. Rondelez, “Dynamics of Dewetting,” *Phys. Rev. Lett.*, vol. 66, no. 6, pp. 715–718, Feb. 1991.
[10] F. Brochard-Wyart and C. Redon, “Dynamics of liquid rim instabilities,” *Langmuir*, vol. 8, no. 9, pp. 2324–2329, Sep. 1992.
[11] U. Thiele, M. Mertig, and W. Pompe, “Dewetting of an Evaporating Thin Liquid Film: Heterogeneous Nucleation and Surface Instability,” *Phys. Rev. Lett.*, vol. 80, no. 13, pp. 2869–2872, Mar. 1998.
[12] M. Nič, J. Jirát, B. Košata, A. Jenkins, and A. McNaught, Eds., “spinodal decomposition,” in *IUPAC Compendium of Chemical Terminology*, 2.1.0., Research Triagle Park, NC: IUPAC, 2009.
[13] C. Favazza, R. Kalyanaraman, and R. Sureshkumar, “Robust nanopatterning by laser-induced dewetting of metal nanofilms,” *Nanotechnology*, vol. 17, no. 16, p. 4229, 2006.
[14] S. P. Singh, “Spinodal Theory: A Common Rupturing Mechanism in Spinodal Dewetting and Surface Directed Phase Separation (Some Technological Aspects: Spatial Correlations and the Significance of Dipole-Quadrupole Interaction in Spinodal Dewetting),” *Adv. Condens. Matter Phys.*, vol. 2011, p. e526397, May 2011.
[15] J. T. McKeown *et al.*, “Real-Time Observation of Nanosecond Liquid-Phase Assembly of Nickel Nanoparticles via Pulsed-Laser Heating,” *Langmuir*, vol. 28, no. 49, pp. 17168–17175, Dec. 2012.
[16] T. Driessen, R. Jeurissen, H. Wijshoff, F. Toschi, and D. Lohse, “Stability of viscous long liquid filaments,” *Phys. Fluids*, vol. 25, no. 6, p. 062109, Jun. 2013.
[17] J. Fowlkes, S. Horton, M. Fuentes-Cabrera, and P. D. Rack, “Signatures of the Rayleigh-Plateau Instability Revealed by Imposing Synthetic Perturbations on Nanometer-Sized Liquid Metals on Substrates,” *Angew. Chem. Int. Ed.*, vol. 51, no. 35, pp. 8768–8772, Aug. 2012.

[18] J. T. McKeown, Y. Wu, J. D. Fowlkes, P. D. Rack, and G. H. Campbell, “Simultaneous In-Situ Synthesis and Characterization of Co@Cu Core-Shell Nanoparticle Arrays,” *Adv. Mater.*, vol. 27, no. 6, pp. 1060–1065, Feb. 2015.
[19] J. D. Fowlkes, L. Kondic, J. Diez, Y. Wu, and P. D. Rack, “Self-Assembly versus Directed Assembly of Nanoparticles via Pulsed Laser Induced Dewetting of Patterned Metal Films,” *Nano Lett.*, vol. 11, no. 6, pp. 2478–2485, Jun. 2011.
[20] H. Krishna, R. Sachan, J. Strader, C. Favazza, M. Khenner, and R. Kalyanaraman, “Thickness-dependent spontaneous dewetting morphology of ultrathin Ag films,” *Nanotechnology*, vol. 21, no. 15, p. 155601, 2010.
[21] Y. Wu, J. D. Fowlkes, and P. D. Rack, “The optical properties of Cu-Ni nanoparticles produced via pulsed laser dewetting of ultrathin films: The effect of nanoparticle size and composition on the plasmon response,” *Journal of Materials Research*, Jan-2011. [Online]. Available: /core/journals/journal-of-materials-research/article/optical-properties-of-cuni-nanoparticles-produced-via-pulsed-laser-dewetting-of-ultrathin-films-the-effect-of-nanoparticle-size-and-composition-on-the-plasmon-response/740668C01ED0F3ED0E409E24C247ECAF/core-reader. [Accessed: 04-Apr-2017].
[22] Y. Wu *et al.*, “Directed Liquid Phase Assembly of Highly Ordered Metallic Nanoparticle Arrays,” *ACS Appl. Mater. Interfaces*, vol. 6, no. 8, pp. 5835–5843, Apr. 2014.
[23] K. M. M. Abou El-Nour, A. Eftaiha, A. Al-Warthan, and R. A. A. Ammar, “Synthesis and applications of silver nanoparticles,” *Arab. J. Chem.*, vol. 3, no. 3, pp. 135–140, Jul. 2010.
[24] S.-H. Wu and D.-H. Chen, “Synthesis and characterization of nickel nanoparticles by hydrazine reduction in ethylene glycol,” *J. Colloid Interface Sci.*, vol. 259, no. 2, pp. 282–286, Mar. 2003.
[25] P. Prieto, V. Nistor, K. Nouneh, M. Oyama, M. Abd-Lefdil, and R. Díaz, “XPS study of silver, nickel and bimetallic silver–nickel nanoparticles prepared by seed-mediated growth,” *Appl. Surf. Sci.*, vol. 258, no. 22, pp. 8807–8813, Sep. 2012.
[26] J. A. Adekoya, E. O. Dare, M. A. Mesubi, and N. Revaprasadu, “Synthesis and Characterization of Optically Active Fractal Seed Mediated Silver Nickel Bimetallic Nanoparticles,” *J. Mater.*, vol. 2014, p. e184216, Mar. 2014.
[27] M. B. Gawande *et al.*, “Core–shell nanoparticles: synthesis and applications in catalysis and electrocatalysis,” *Chem. Soc. Rev.*, vol. 44, no. 21, pp. 7540–7590, Oct. 2015.
[28] X. J. Liu, F. Gao, C. P. Wang, and K. Ishida, “Thermodynamic Assessments of the Ag-Ni Binary and Ag-Cu-Ni Ternary Systems,” *J. Electron. Mater.*, vol. 37, no. 2, pp. 210–217, Feb. 2008.
[29] M. McCord and M. Rooks, “SPIE Handbook, Volume 1: Microlithography, Section 2.1.” [Online]. Available: http://www.cnf.cornell.edu/cnf_spie1.html#2.1.1. [Accessed: 02-Mar-2017].
[30] S. Sedky *et al.*, “Microencapsulation of silicon cavities using a pulsed excimer laser,” *J. Micromechanics Microengineering*, vol. 22, no. 7, p. 075012, 2012.
[31] M. Hughes, “What Is Thin Film Deposition?,” *Semicore*, 21-Nov-2014. [Online]. Available: http://www.semicore.com/news/81-what-is-thin-film-deposition. [Accessed: 02-Mar-2017].
[32] Indium Corporation, “Chemical Vapor Deposition vs. Physical vapor deposition.” 2008.
[33] AJA International, “What is sputtering?,” *AJA International*. [Online]. Available: http://www.ajaint.com/what-is-sputtering.html. [Accessed: 06-Apr-2017].

[34] Semicore, “What is RF Sputtering?” [Online]. Available: http://www.semicore.com/news/92-what-is-rf-sputtering. [Accessed: 06-Apr-2017].
[35] C. Srivastava, S. Chithra, K. D. Malviya, S. K. Sinha, and K. Chattopadhyay, “Size dependent microstructure for Ag–Ni nanoparticles,” *Acta Mater.*, vol. 59, no. 16, pp. 6501–6509, Sep. 2011.
[36] S. J. Henley, J. D. Carey, and S. R. P. Silva, “Pulsed-laser-induced nanoscale island formation in thin metal-on-oxide films,” *Phys. Rev. B*, vol. 72, no. 19, p. 195408, Nov. 2005.
[37] J. Trice, D. Thomas, C. Favazza, R. Sureshkumar, and R. Kalyanaraman, “Pulsed-laser-induced dewetting in nanoscopic metal films: Theory and experiments,” *Phys. Rev. B*, vol. 75, no. 23, p. 235439, Jun. 2007.
[38] F. Ruffino *et al.*, “Novel approach to the fabrication of Au/silica core–shell nanostructures based on nanosecond laser irradiation of thin Au films on Si,” *Nanotechnology*, vol. 23, no. 4, p. 045601, 2012.
[39] A. Acharya, “The study of Nucleation Dynamics of Silver Nanoparticles. (PDF Download Available),” *ResearchGate*.
[40] G. Reiter, “Dewetting of thin polymer films,” *Phys. Rev. Lett.*, vol. 68, no. 1, pp. 75–78, Jan. 1992.
[41] H. Krishna, N. Shirato, C. Favazza, and R. Kalyanaraman, “Energy driven self-organization in nanoscale metallic liquid films,” *Phys. Chem. Chem. Phys.*, vol. 11, no. 37, pp. 8136–8143, Sep. 2009.
[42] P. Krishnakumar, “Wetting and spreading phenomena.” 13-May-2010.
[43] J. N. Israelachvili, “Chapter 13 - Van der Waals Forces between Particles and Surfaces,” in *Intermolecular and Surface Forces (Third Edition)*, San Diego: Academic Press, 2011, pp. 253–289.
[44] J. J. Jing, J. M. Xie, H. R. Qin, W. H. Li, and M. M. Zhang, “Preparation and Characterization of Nickel(Ni)-Silver(Ag) Core-Shell Nanoparticles for Conductive Pastes,” *Adv. Mater. Res.*, vol. 531, pp. 211–214, 2012.
[45] K. S. Kumar, V. B. Kumar, and P. Paik, “Recent Advancement in Functional Core-Shell Nanoparticles of Polymers: Synthesis, Physical Properties, and Applications in Medical Biotechnology,” *J. Nanoparticles*, vol. 2013, Jan. 2013.
[46] SGTE - Scientific Group Thermodata Europe, “Ni-Ag Binary Phase Diagram.” [Online]. Available: http://www.crct.polymtl.ca/sgte/index.php?what=1&databases=1&nobl=1. [Accessed: 01-Mar-2017].
[47] M. A. Mohammad, M. Muhammad, S. K. Dew, and M. Stepanova, “Fundamentals of Electron Beam Exposure and Development,” in *Nanofabrication*, M. Stepanova and S. Dew, Eds. Springer Vienna, 2012, pp. 11–41.
[48] D. Sands, *Pulsed Laser Heating and Melting*. INTECH Open Access Publisher, 2011.
[49] A. Majeed, J. He, L. Jiao, X. Zhong, and Z. Sheng, “Surface properties and biocompatibility of nanostructured TiO2 film deposited by RF magnetron sputtering,” *Nanoscale Res. Lett.*, vol. 10, 2015.
[50] E. Alfonso, J. Olaya, and G. Cubillos, “Thin Film Growth Through Sputtering Technique and Its Applications,” 2012.
[51] “SelfAssembly_EncyclopediaMaterials.pdf.” .
[52] “Sputter deposition - LNF Wiki.” [Online]. Available: http://lnf-wiki.eecs.umich.edu/wiki/Sputter_deposition. [Accessed: 06-Apr-2017].

[53] NPTEL, “Advances in Spintronic Materials, Technology and Devices.” [Online]. Available: http://nptel.ac.in/courses/115103039/module16/lec39/1.html. [Accessed: 06-Apr-2017].
[54] M. Harb, F. Rabilloud, and D. Simon, “Structure and optical properties of core-shell bimetallic AgnNin clusters: Comparison with pure silver and nickel clusters,” *J. Chem. Phys.*, vol. 131, no. 17, p. 174302, Nov. 2009.
[55] F. Baletto, C. Mottet, A. Rapallo, G. Rossi, and R. Ferrando, “Growth and energetic stability of AgNi core-shell clusters,” *Surf. Sci.*, vol. 566, no. 1–3 PART 1, pp. 192–196, Sep. 2004.
[56] D. Josell and F. Spaepen, “Determination of the interfacial tension by zero creep experiments on multilayers—I. Theory,” *Acta Metall. Mater.*, vol. 41, no. 10, pp. 3007–3015, Oct. 1993.
[57] K. D. Malviya and K. Chattopadhyay, “Synthesis and Mechanism of Composition and Size Dependent Morphology Selection in Nanoparticles of Ag–Cu Alloys Processed by Laser Ablation Under Liquid Medium,” *J. Phys. Chem. C*, vol. 118, no. 24, pp. 13228–13237, Jun. 2014.
[58] K. S. Gadre and T. L. Alford, “Contact angle measurements for adhesion energy evaluation of silver and copper films on parylene-n and SiO2 substrates,” *J. Appl. Phys.*, vol. 93, no. 2, pp. 919–923, Dec. 2002.
[59] D. C. Sundberg and Y. G. Durant, “Latex Particle Morphology, Fundamental Aspects: A Review,” *Polym. React. Eng.*, vol. 11, no. 3, pp. 379–432, Jan. 2003.
[60] E. A. A. Jarvis and E. A. Carter, “Exploiting Covalency to Enhance Metal–Oxide and Oxide–Oxide Adhesion at Heterogeneous Interfaces,” *J. Am. Ceram. Soc.*, vol. 86, no. 3, pp. 373–386, Mar. 2003.

Vita

Ben Wolf was born on March 17, 1993 in Dallas, Texas to his parents Robert and Darlene Wolf. He attended Lake Highlands High school where he was a class officer and baseball player and graduated in 2011. Ben then attended the University of Virginia in Charlottesville, Virginia where he was a member of the fraternity of Phi Gamma Delta and received a degree in Nano-Medicine in 2015. During his time at the University of Virginia, Ben fostered his interests in technology entrepreneurship and decided to attend the University of Tennessee in Knoxville, Tennessee to exercise these interests. Ben received his Master's degree in Materials Science and Engineering from the University of Tennessee in August 2017.